Available online at www.sciencedirect.com

ScienceDirect

Green Energy & Environment 3 (2018) 335–351

www.keaipublishing.com/gee

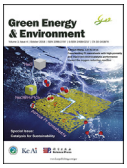

Review article

# Electrocatalysts based on metal@carbon core@shell nanocomposites: An overview

Yi Peng, Shaowei Chen*

*Department of Chemistry and Biochemistry, University of California, 1156 High Street, Santa Cruz, CA 95064, USA*

Received 28 June 2018; revised 24 July 2018; accepted 27 July 2018
Available online 23 August 2018

**Abstract**

Developing low-cost, high-performance catalysts is of fundamental significance for electrochemical energy conversion and storage. In recent years, metal@carbon core@shell nanocomposites have emerged as a unique class of functional nanomaterials that show apparent electrocatalytic activity towards a range of reactions, such as hydrogen evolution reaction, oxygen evolution reaction, oxygen reduction reaction, and $CO_2$ reduction reaction, that are important in water splitting, fuel cells and metal-air batteries. The activity is primarily attributed to interfacial charge transfer from the metal core to the carbon shell that manipulate the electronic interactions between the catalyst surface and reaction intermediates, and varies with the structures and morphologies of the metal core (elemental composition, core size, etc.) and carbon shell (doping, layer thickness, etc.). Further manipulation can be achieved by the incorporation of a third structural component. A perspective is also included highlighting the current gap between theoretical modeling and experimental results, and technical challenges for future research.


*Keywords:* Metal@carbon core@shell nanocomposite; Electrocatalysis; Hydrogen evolution reaction; Oxygen evolution reaction; Oxygen reduction reaction

## 1. Introduction

In recent decades, extensive research efforts have been devoted to the development of effective technologies for electrochemical energy conversion and storage, which entail, in particular, rational design and engineering of functional nanomaterials as high-performance, low-cost catalysts towards important reactions, such as hydrogen evolution reaction (HER), oxygen evolution reaction (OER), oxygen reduction reaction (ORR), and carbon dioxide reduction reaction ($CO_2$RR) [1–7]. Currently, the leading catalysts for these reactions are generally based on noble metals such as platinum, ruthenium and iridium [8–12], where structural engineering represents a key strategy to enhance the performance and concurrently reduce the costs of the catalysts [13–18]. This has been demonstrated in a number of prior studies that focus on the manipulation of the elemental compositions, crystalline facets, surface morphologies, as well as alloying of the nanoparticles with (non-)noble metals [19–26]. In some other studies [2,27–31], nanocomposites based on (non-noble) metals and metal compounds incorporated into carbon matrices have also been found to exhibit apparent electrocatalytic activity. For instance, Wang and coworkers [2] summarized non-noble metal-based carbon composites as HER electrocatalysts and the activity was attributed to (i) improved electrical conductivity by the carbon phase and texture structures, (ii) the formation of abundant active sites due to high dispersion of small-sized metal/metal composites on carbon, and (iii) charge transfer dynamics facilitated by the synergistic coupling between the two components. The Chen group [31] reviewed single metal atoms supported on a carbon matrix as efficient electrocatalysts, and Asefa et al. [27] summarized (noble) metal-free heteroatom-doped carbons as high-performance electrocatalysts. Among these,

* Corresponding author.
*E-mail address:* shaowei@ucsc.edu (S. Chen).

https://doi.org/10.1016/j.gee.2018.07.006

metal@carbon (M@C) core@shell composites, where metal nanoparticles are encapsulated within a carbon matrix, have been attracting particular interest because of their unique features, such as high electrical conductivity, large surface area, and optimizable surface electronic structure due to intimate interactions between the metal core and carbon shell [32–35]. The encapsulation of the metal nanoparticles within a carbon shell also leads to enhanced structural stability of the metal and thus long-term durability of the catalysts [36–46]. In this review, we will focus on recent progress in the design and engineering of M@C electrocatalysts towards diverse reactions (Fig. 1), within the context of the metal cores, carbon shells, and third components.

We will start with an overview of theoretical advances that help develop a mechanistic framework of M@C composites in electrocatalysis, summarize recent progress in the design and engineering of various M@C structures for diverse applications, and then include a perspective that highlights key challenges in future research.

## 2. Mechanistic framework

To rationally design high-performance, advanced electrocatalysts, it is of fundamental importance to understand the reaction pathways and identify catalytic active sites, in which density functional theory (DFT) calculations have been playing a powerful role [47–52]. For instance, M@C nanocomposites have been known to be active towards HER, which in general entails three key reactions in acid,

$$\text{Volmer reaction: } * + H^+ + e^- \leftrightarrow H* \quad (1)$$

$$\text{Tafel reaction: } 2H* \leftrightarrow H_2* \quad (2)$$

$$\text{Heyrovsky reaction: } * + H^+ + e^- + H* \leftrightarrow H_2* \quad (3)$$

where * is the active site of the catalyst. Results from DFT calculations have shown that the HER process likely involves the Volmer–Heyrovsky or Volmer–Tafel pathway on a range of transition-metal surfaces, where the Volmer step is a fast reaction while the Heyrovsky or Tafel reaction is the rate-determining step [53–55]. In 1958, Parson first pointed out that a maximum exchange current density would be attained when the hydrogen adsorption free energy ($\Delta G_{H*}$) was close to thermoneutral ($\Delta G_{H*} \sim 0$) [56]. Norskov et al. plotted $\Delta G_{H*}$ from DFT calculations versus experimental HER exchange current density (Fig. 2) [57], and observed a volcano-shaped variation with the peak position close to platinum—note that platinum is the state-of-the-art HER catalyst with an almost zero overpotential and small Tafel slope. This volcano plot was further consummated in other studies in the literatures [58,59]. This suggests that $\Delta G_{H*}$ can be exploited as an effective descriptor in the design, engineering and optimization of HER catalysts. For M@C catalysts, with the active sites located on the carbon shell, one can see that whereas $\Delta G_{H*}$ on pure C is very positive and $H^+$ adsorption (Volmer step) is energetically unfavorable, in contrast to transition metals where $\Delta G_{H*}$ is generally negative, the formation of M@C core@shell structures leads to reduced $\Delta G_{H*}$ on the C shell, in good agreement with enhanced HER activity observed experimentally. This is largely attributed to effective

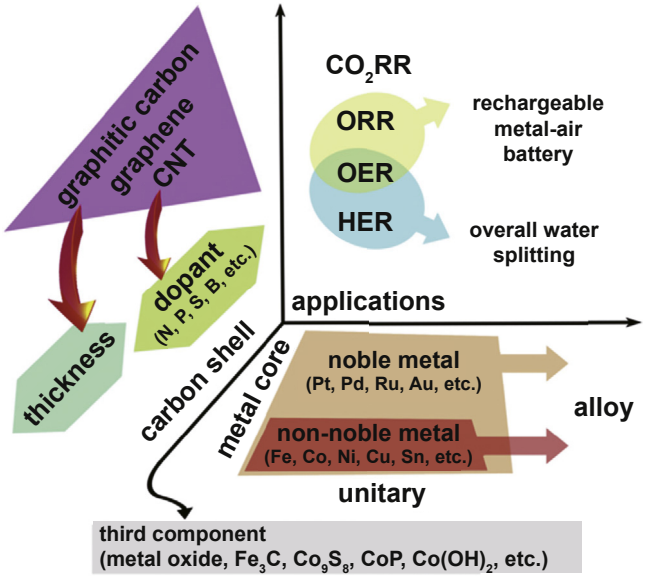


Fig. 1. An overview illustration of M@C composites, where the metal core can be a noble metal (Pt, Pd, Ru, Au, etc), non-noble metal (Fe, Co, Ni, Cu, Sn, etc.), or their alloy, and the carbon shell varies in thickness, ranging from carbon nanotube (CNT), to graphene, and graphitic carbon with or without dopants (N, P, S, B, etc). These catalysts can be used for ORR, OER, HER and $CO_2RR$, and devices like overall water splitting and rechargeable metal-air battery. A third component material like metal oxide, $Fe_3C$, $Co_9S_8$, CoP, $Co(OH)_2$, etc, can also be integrated as part of the core or shell, or with the M@C materials forming a more complicated composite structure with a further enhanced performance.

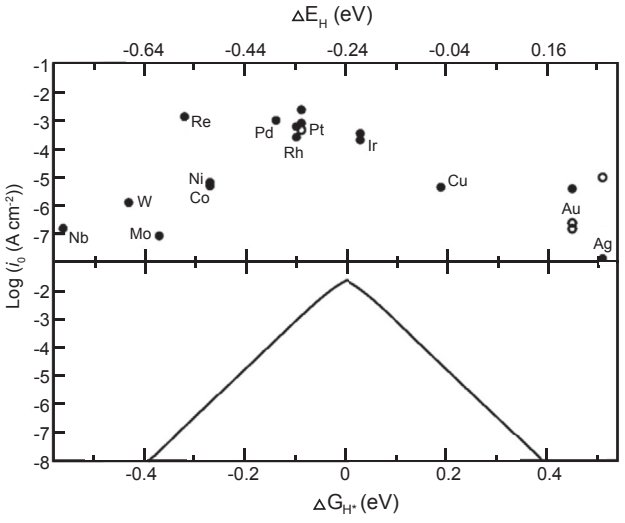


Fig. 2. Experimental results of exchange current density ($i_0$) of HER over different metal surfaces plotted as a function of calculated Gibbs free energy of hydrogen adsorption per atom ($\Delta E_H$, top axis) and the fitted volcano plot as a function of Gibbs free energy of hydrogen adsorption ($\Delta G_{H*}$, bottom axis). $\Delta G_{H*} = \Delta E_H + 0.24$ eV (Reproduced with permission from Ref. [57] ©2005 The Electrochemical Society).

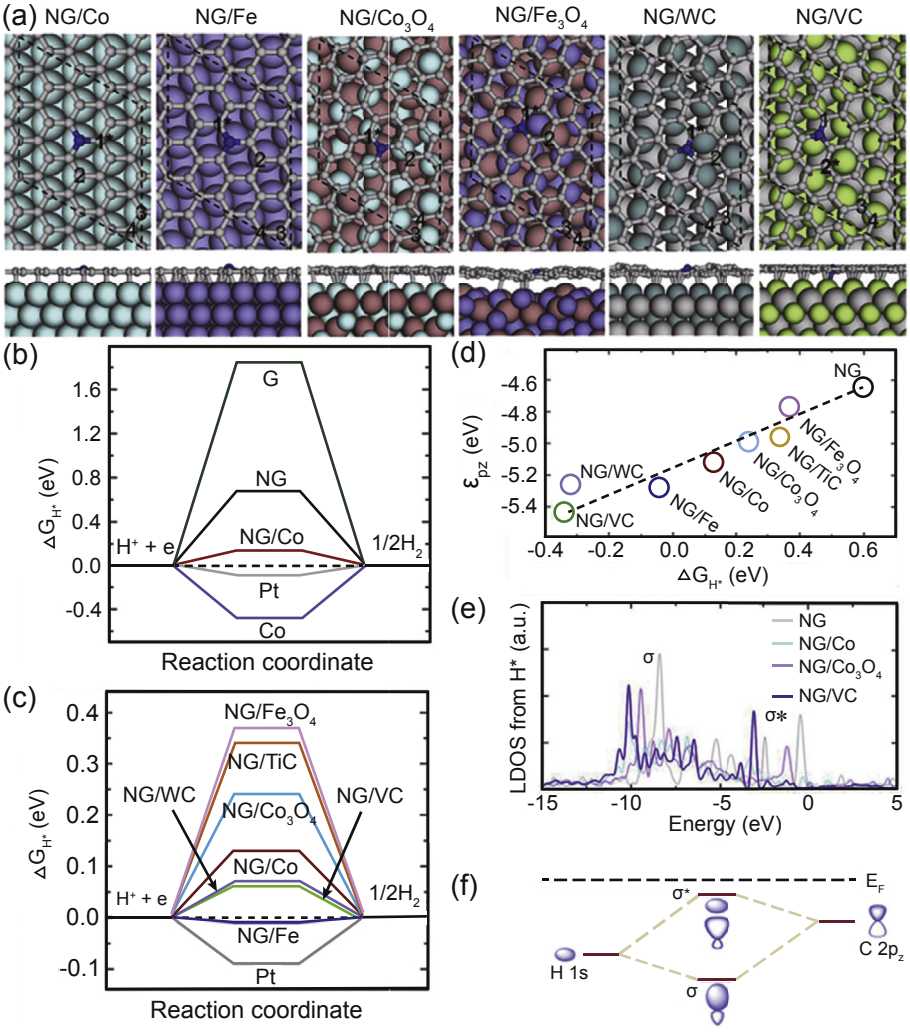


Fig. 3. (a) Top and side views of N-doped graphene on various substrates. (b–c) Free energy diagrams for HER at zero potential and pH = 0 on G, NG, Co, NG/Co and Pt surfaces, and NG on various substrates. (d) The plot of C $p_z$ center versus $\Delta G_{H^*}$ of different hybrids. (e) LDOS of a H atom adsorbed on the active sites of various hybrids. (f) Schematic illustration of H–C bonds formation on the hybrids (Reproduced with permission from Ref. [61] ©2018 Elsevier).

charge transfer from the metal core to the carbon shell [60]. Further contributions can arise from deliberate doping of the carbon shells by select metal and nonmetal heteroatoms. Fig. 3 depicts results from DFT calculations of N-doped graphitic carbon hybridized with various transition metals (compounds) in HER electrocatalysis [61]. The atomic structures of the hybrids of N-doped graphene (NG) supported on substrates like Co (111), Fe (110), $Co_3O_4$ (111), $Fe_3O_4$ (111), WC (0001) and VC (111) are illustrated in Fig. 3a, with the corresponding $\Delta G_{H^*}$ shown in Fig. 3b. One can see that $\Delta G_{H^*}$ of undoped graphene (G) is very positive at +1.84 eV, suggesting difficult adsorption of proton. Introduction of N dopants into G (NG) markedly lowers the $\Delta G_{H^*}$ to +0.54 eV. For comparison, $\Delta G_{H^*}$ is −0.48 eV on Co (111); and in the NG/Co hybrid, $\Delta G_{H^*}$ is reduced to +0.13 eV on the C sites adjacent to N dopant and on the hollow site of Co substrate, a condition favored for HER. Fig. 3c further compares the $\Delta G_{H^*}$ of NG on other substrates, where the proton binding strength can be seen to follow the order of NG/Fe > NG/VC ~ NG/WC > NG/Co > NG/$Co_3O_4$ > NG/$Fe_3O_4$ ~ NG/TiC. This is accounted for by electron injection from the substrates to the graphitic sheet that breaks the π conjugation by occupying the carbon $p_z$ orbitals. This can be described by the center of the C $p_z$ band by the following equation, $\varepsilon p_z = \int_{-\infty}^{0} ED(E)\,dE / \int_{-\infty}^{0} D(E)\,dE$, where D(E) is the DOS of the C $p_z$ band at a given energy. Interestingly, the $\varepsilon p_z$ values of the hybrids show a linear relationship with the corresponding $\Delta G_{H^*}$ (Fig. 3d), suggesting that a lower C $p_z$ band center can strengthen proton binding. Note this is in contrast with the results of proton adsorption onto transition metal surfaces described by the d-band center theory [62], because of the full occupancy of the σ* orbitals of H* and C when protons are adsorbed on carbon active sites, where few electronic states can be found in the conduction bands (Fig. 3e–f). Therefore, the bonding with proton will be strengthened with a deeper valence orbital level of the graphitic sheet. From these DFT calculations, one can see that indeed dopants and substrate interactions play an important role in boosting the activity of

carbon towards HER by charge transfer from the substrate to carbon.

Such interfacial charge transfer is also responsible for electrocatalytic activity towards other reactions, such as OER and ORR. Here we will focus on OER [63–67], as ORR is the reverse of OER and has been widely studied [68–72]. Generally, OER in alkaline media involves four steps as described below [65],

$$* + OH^- \leftrightarrow HO* + e^- \qquad \Delta G(HO*) \qquad (4)$$

$$HO* + OH^- \leftrightarrow H_2O + O* + e^- \qquad \Delta G(O*) \qquad (5)$$

$$O* + OH^- \leftrightarrow HOO* + e^- \qquad \Delta G(HOO*) \qquad (6)$$

$$HOO* + OH^- \leftrightarrow * + O_2 + H_2O + e^- \qquad \Delta G(*) \qquad (7)$$

The overall reaction energy $\Delta G^{OER} = \Delta G(HO*) + \Delta G(O*) + \Delta G(HOO*) + \Delta G(*)$, which is a constant. Here we take FeNi@C [35] as an illustrating example. Fig. 4a schematically illustrates a FeNi@C model for DFT calculation and the adsorption of various oxygen intermediates. Fig. 4b plots the Gibbs free energies at different reaction stages under various potentials, from which an overpotential of 0.49 V is suggested to catalyze OER on FeNi@C, as compared to the equilibrium potential (1.23 V). Extending the studies to other M@C samples involving a range of metal nanoparticles (Fig. 4c), one can see that there is a good scaling relationship between G(HO*) and ΔG(HOO*) with an intercept of 3.2 eV and a slope of 1 [65], indicating that HO* and HOO* likely follow the same bonding mechanism to the catalyst surface. The overpotential can be readily determined by the difference of the binding free energy between O* and HO*, ΔG(O*) − ΔG(HO*). Using this as an activity descriptor, one can see that the plot of calculated overpotential versus ΔG(O*)−ΔG(HO*) displays a volcano feature (Fig. 4d), and that of FeNi@C is ca. 1.48 eV, closest to the volcano peak, which suggests that FeNi@C is the most active one among the series of samples. This is indeed confirmed by experimental studies. Figs. 4e–f display the representative TEM and HRTEM images of FeNi@NC, where FeNi nanoparticles of 6–10 nm (with well-defined lattice fringes) are encapsulated within a single layer graphene shell. Electrochemical measurements (Figs. 4g–h) show that the OER performance of the series of M@NC catalysts follows the order of FeNi > CoNi > FeCo > Ni > Co > Fe, by comparing the electrode potentials needed to reach the current density of 10 mA $cm^{-2}$ ($E_{10}$). This is, again, ascribed to electron transfer from the metal core to the carbon shell that manipulates the ΔG of reaction intermediates, specifically, ΔG(O*) − ΔG(HO*). In fact, the number of electrons gained per metal atom is 0.15, 0.12, 0.07 and 0.10 for Fe@C, Co@C, Ni@C and FeNi@C, respectively, where the corresponding ΔG(O*) − ΔG(HO*) increases to 1.03, 1.06, 1.21 and 1.48 eV, as compared to that of pristine graphene. The best sample, FeNi@NC, also shows excellent durability, as compared to the benchmark $IrO_2$ catalyst when tested at the current density of 40 and 100 mA $cm^{-2}$ for 10,000 cycles (Fig. 4h), consistent with results from the DFT calculations.

## 3. Metal core effect

As demonstrated above, interfacial charge transfer from the metal core to the carbon shell is argued to be the main driving

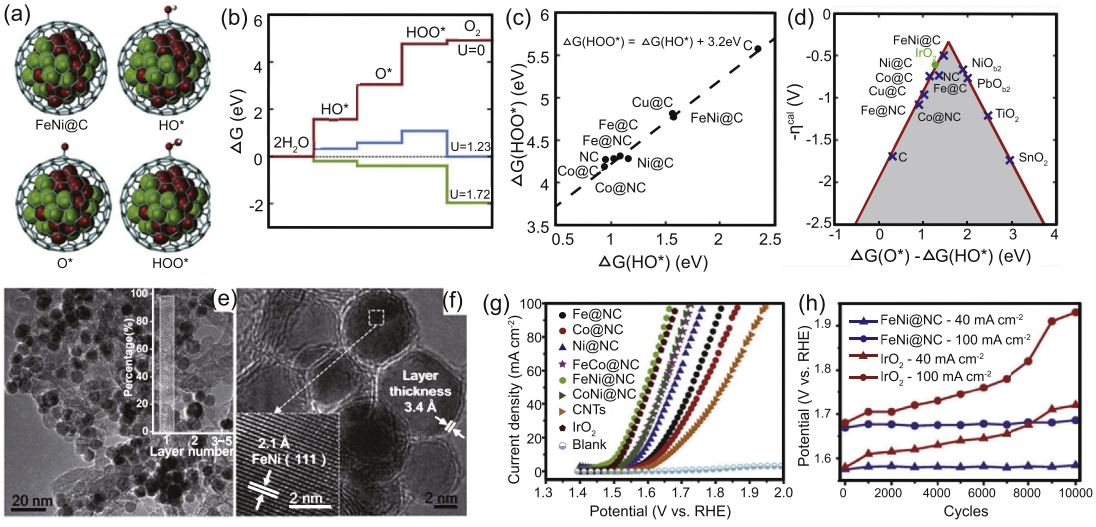


Fig. 4. (a) Schematic model of FeNi@NC and OER steps on the catalyst. (b) Free energy profiles for OER on FeNi@C at different potentials. (c) Linear relationship of free energy of HO* (ΔG(HO*)) versus HOO* (ΔG(HOO*)). (d) Overpotential ($\eta^{cal}$) based on DFT calculation against the universal descriptor ΔG(O*)−ΔG(HO*). The data of metal oxides were cited from literature [73]. (e) TEM image of FeNi@NC, and inset is the corresponding histogram of the layer number of the graphene shell. (f) HRTEM image of FeNi@NC, and inset is the lattice fringes of FeNi alloy (111) crystalline phase. (g) OER performance of FeNi@NC and other catalysts. (h) Comparison of stability test of FeNi@NC with $IrO_2$ via potential changes at the constant current density of 40 or 100 mA $cm^{-2}$ (Reproduced with permission from Ref. [35] ©2016 Royal Society of Chemistry).

force responsible for the electrocatalytic activity of M@C composites. Within this fundamental framework, one can see that the electrocatalytic activity can be readily manipulated by the metal work functions [74,75], which depends on the chemical nature of the metals (Table 1), as well as elemental composition and arrangement of metal alloys (Table 2). In an early study with metal nanoparticles encapsulated in N-doped graphene (M@NG) [45], the HER activity was indeed found to vary with the elemental composition of the metal nanoparticles. Figs. 5a–c depict the HRTEM images of RuCo@NG (3.58 wt% Ru), where one can see that the RuCo nanoalloy particles are encapsulated within a carbon shell of 6–15 graphene layers in thickness, and the cubic and hexagonal Co phases can be clearly identified from the lattice fringes, while no Ru phase can be observed due to the low content. Fig. 5d compares the HER performance of the resulting RuCo@NG, Ru nanoparticles, and Pt/C in 1 M KOH. It can be seen that the RuCo@NG sample shows an overpotential ($\eta_{10}$) of only −28 mV to reach the current density of 10 mA $cm^{-2}$, a performance even better than that of Pt/C ($\eta_{10} = -40$ mV) or Ru nanoparticles ($\eta_{10} = -58$ mV). Also, RuCo@NG exhibits great long-term stability since $\eta_{10}$ only increases by 4 mV after 10,000 cycles, while $\eta_{10}$ of Pt/C increases by 8 mV and that of Ru nanoparticles increases much more dramatically by almost 70 mV (Fig. 5d). Results from DFT calculations (Fig. 5e) show that $|\Delta G_H^*|$ decreases gradually with the increase of Ru content in $Ru_xCo_{55-x}@N_1C_{239}$ (x = 0, 1, 2, or 3), suggesting that the improved HER performance is likely due to enhanced proton adsorption. Furthermore, from the charge density distribution of $Co_{55}@N_1C_{239}$ and $Ru_3Co_{52}@N_1C_{239}$ (Fig. 5f), the Bader charge transfer number from the metal core to the graphene shell can be estimated to be 5.81 and 5.91, respectively, consistent with the higher HER activity observed with RuCo@NG than with Co@NG, likely due to the strengthening of the C−H bond. Certainly one may notice that in the experimental studies the particles are much larger (~30 nm), and the graphene layers much thicker (6–15 layers). This raises serious questions about the direct correlation between the results from the experimental and theoretical studies. Nevertheless, both results suggest that indeed the

Table 1
Summary of electrocatalytic performances of single-metal M@C nanocomposites.

| Metal core | Carbon shell | Electrolyte | Electrocatalytic Performance[a] | Ref. |
|---|---|---|---|---|
| Co | C | 1.0 M KOH | Overall water splitting: $E_{10ws}$ = 1.653 V | [81] |
| Co | Co, N, S−G | 1.0 M KOH | HER: $\eta_{10}$ = −247 mV; OER: $\eta_{10}$ = +337 mV | [82] |
| Co | N−C | 0.5 M $H_2SO_4$ (0.1 M NaOH) | HER : $\eta_{10}$ = −265 mV (−337 mV) | [36] |
| Co | N−C | 0.5 M $H_2SO_4$ (1.0 M KOH) | HER: $\eta_{10}$ = −82 mV (−95 mV); ORR: $E_{1/2}$ = 0.78 V (0.9 V) | [37] |
| Co | N−CNT | 0.5 M $H_2SO_4$ | HER: $\eta_{10}$ = −215 mV | [38] |
| Co | N−CNT | 0.1 M KOH (1.0 M PBS) | OER: $\eta_{50}$ = 300 mV ($\eta_{10}$ = 310 mV); ORR: $E_{onset}$ = 0.8 V (0.75 V) | [83] |
| Cu | N−C | 0.1 M KOH | ORR: $E_{1/2}$ = −0.24 V vs SCE, $E_{onset}$ = −0.06 V vs SCE | [84] |
| Co | B, N−C | 0.5 M $H_2SO_4$ (1.0 M KOH) | HER: $\eta_{10}$ = −96 mV (−183 mV) | [39] |
| Ni | G | 1.0 M KOH | HER: $\eta_{10}$ = −240 mV; OER: $\eta_{10}$ = +370 mV | [85] |
| Co | N−C/N−rGO | 0.1 M KOH | ORR: $E_{onset}$ = 0.94 V; HER: $\eta_{10}$ = −229 mV; OER: $\eta_{10}$ = 430 mV | [86] |
| Co | N−G | 0.5 M $H_2SO_4$ (1.0 M KOH) | ORR: $E_{onset}$ = 0.77 V (0.90 V), $E_{1/2}$ = 0.55 (0.83 V); HER: $\eta_{10}$ = −183 mV (−220 mV) | [87] |
| Co | N−C | 0.1 M KOH | ORR: $E_{onset}$ = −0.08 V, $E_{1/2}$ = −0.15 V vs Ag/AgCl (3.5 M KCl) | [88] |
| Co | N−CNT | 0.5 M $H_2SO_4$ | HER: $\eta_{10}$ = −280 mV | [40] |
| Fe | N−CNT | | $H_2$−$O_2$ fuel cell: 60% voltage of Pt/C | [89] |
| Co | N−CNT | Universal pH | HER: $\eta_{10}$ = −103/−337/−204 mV at pH = 0/7/14 | [90] |
| Co | N−CNT | 0.1 M KOH | ORR: $E_{onset}$ = 0.929 V, $E_{1/2}$ = 0.849 V | [91] |
| Co | N−CF | 0.5 M $H_2SO_4$ | HER: $\eta_{10}$ = −61 mV | [41] |
| Co | rGO | 0.1 M KOH | ORR: $E_{onset}$ = −0.01 V vs. SCE | [92] |
| Co | N−C/CNT | 1.0 M KOH | Overall water splitting: $E_{10ws}$ = 1.625 V | [93] |
| Co | N−CF | 1.0 M KOH | Overall water splitting: $E_{10ws}$ = 1.66 V | [94] |
| Co | N−G | 0.5 M $H_2SO_4$ | HER: $\eta_{10}$ = −125 mV | [42] |
| Cu | N−C | 0.1 M KOH | ORR: $E_{onset}$ = +0.94 V, $E_{1/2}$ = 0.83 V | [95] |
| Ni | N−C | 1.0 M KOH | HER: $\eta_{20}$ = −88 mV | [96] |
| Co | N−CNT | 0.1 M KOH | Oxygen electrode: ΔE = 0.78 V | [97] |
| Co | N−G | 0.1 M KOH | ORR: $E_{onset}$ = −0.035 V vs. SCE | [98] |
| Co | N−GR/C | 0.1 M KOH | ORR: $E_{1/2}$ = 0.83 V | [99] |
| Co | N−G | 1.0 M $LiClO_4$−DMSO | Li−Oxygen battery: 0.58 V overpotential | [100] |
| Co | NC@GC | 0.1 M KOH | Oxygen electrode: ΔE = 0.64 V | [101] |
| Co | N−C | 0.1 M KOH | Oxygen electrode: ΔE = 0.859 V | [102] |
| Sn | G | 0.1 M $NaHCO_3$ | $CO_2$RR: 21.1 mA $cm^{-2}$ at −1.8 V vs. SCE | [103] |
| Co | N−CNT | 0.5 M $H_2SO_4$ (1.0 M KOH) | HER: $\eta_{10}$ = −280 mV (−240 mV) | [104] |
| Au | N−C | 0.5 M $H_2SO_4$ | HER: $\eta_{10}$ = −130 mV | [105] |
| Au | Zn−Fe−C | 0.5 M $H_2SO_4$ (0.1 M KOH) | HER: $\eta_{10}$ = −123 mV, ORR: $E_{onset}$ = 0.94 V | [106] |

[a] In HER and OER, $\eta_{10}$ refers to the overpotential needed to reach the current density of 10 mA $cm^{-2}$. In ORR, $E_{onset}$ and $E_{½}$ denote onset potential and half-wave potential, respectively. In oxygen electrode, ΔE is the difference between the potential at the OER current density of 10 mA/$cm^2$ and ORR half-wave potential, i.e., $\Delta E = E_{10,OER} - E_{½,ORR}$. In overall water splitting, $E_{10ws}$ is the cell potential needed for a current density of 10 mA/$cm^2$. All the potentials are versus to RHE if there is no special notification.

Table 2
Summary of electrocatalytic performances of alloy M@C nanocomposites.

| Alloy core | Shell | Electrolyte | Electrocatalytic performance | Ref. |
|---|---|---|---|---|
| PdCo | N−C | 0.5 M $H_2SO_4$ | HER: $\eta_{10} = -80$ mV | [44] |
| FeCoNi | N−C | 1.0 M KOH | Water splitting: $E_{10ws} = 1.667$ V | [107] |
| FeNi | N−C | 1.0 M KOH | Water splitting: $E_{10ws} = 1.63$ V; oxygen electrode: $\Delta E = 0.81$ V | [108] |
| NiCu | GC | Universal pH | HER: $\eta_{10} = -48/-164/-74$ mV at pH = 0/7/14 | [109] |
| IrCo | N−C | 0.5 M $H_2SO_4$ | HER: $\eta_{10} = -24$ mV | [46] |
| NiCo | N−C | 0.5 M $H_2SO_4$ | HER: $\eta_{10} = -200$ mV | [60] |
| $Ni_{0.4}Co_{0.6}$ | N−C | 1.0 M KOH | HER: $\eta_{10} = -68$ mV | [110] |
| NiCo | N−C | 0.1 M KOH | ORR: $E_{1/2} = 0.81$ V | [111] |
| NiCo | N−CNT | 0.1 M KOH | ORR: $E_{onset} = 0.93$ V, $E_{1/2} = 0.82$ V | [112] |
| PtPd | N−G | 0.5 M $H_2SO_4$ (0.1 M KOH) | HER: $\eta_{10} = -58$ mV; ORR: $E_{onset} = 0.97$ V | [113] |
| CoNi | N−C | 0.1 M KOH | ORR: $E_{onset} = 0.923$ V, $E_{1/2} = 0.821$ V | [114] |
| FeCoNi | N−C | 0.5 M KOH | OER: $\eta_{10} = 400$ mV | [115] |
| FeCo | N−C | 0.5 M $H_2SO_4$ | HER: $\eta_{10} = -262$ mV | [116] |
| CoNi | N−C | 1.0 M KOH | OER: $\eta_{10} = 280$ mV | [35] |
| PdCo | N−C | 0.1 M KOH | ORR: $E_{onset} = 0.914$ V | [43] |
| NiRu | N−C | Universal pH | HER: $\eta_{10} = -50/-482/-32$ mV at pH = 0/7/14 | [77] |
| NiCo | N−CNT | 0.1 M KOH | OER: $\eta_{10} = 410$ mV | [117] |
| NiCo | PFC | 0.1 M KOH | Oxygen electrode: $\Delta E = 0.86$ V | [118] |
| PtCo | N−C | 0.1 M $HClO_4$ (0.1 M KOH) | ORR: $E_{onset} = 0.929$ V (0.925 V) | [80] |
| NiCo | N−C | 1.0 M KOH | Water splitting: $E_{10ws} = 1.706$ mV | [119] |
| CoRu | N−C | 0.5 M $H_2SO_4$ (1.0 M KOH) | HER: $\eta_{10} = -32$ mV (−45 mV) | [78] |
| RuCo | N−G | 1.0 M KOH | HER: $\eta_{10} = -28$ mV | [45] |
| FeCo | N−G/CNT | 1.0 M KOH | Water splitting: $E_{10ws} = 1.88$ V | [120] |
| FeCo | N−C−KB | 0.5 M $H_2SO_4$ | ORR: $E_{onset} = 0.92$ V, $E_{1/2} = 0.74$ V; HER: $\eta_{10} = -240$ mV | [121] |

encapsulated metal nanoparticles may promote proton adsorption by interfacial charge transfer to the carbon shell. In a more recent study [46], IrCo alloy nanoparticles are encapsulated in N-doped carbon cages at a low Ir content of only 1.56 wt%. Yet the sample shows a better catalytic performance ($\eta_{10} = -24$ mV) in 0.5 M $H_2SO_4$ than Pt/C ($\eta_{10} = -35$ mV). Remarkable HER activity has also been observed with PdCo@NC [44,76], CoRu@NC and NiRu@NC [77,78]. Such M@C nanostructures have also shown apparent activity towards other reactions, such as ORR, ethanol oxidation reaction, and single cell [43,79,80].

Further enhancement of the electrocatalytic performance can be achieved by incorporating a third metal forming more complicated alloy nanoparticles in the catalysts. In an earlier study [107], Yang et al. prepared a series of binary and ternary alloy nanoparticles encapsulated in N-doped carbons and compared the OER and HER activities. Fig. 6a shows a representative HRTEM image of a single FeCoNi@NC nanoparticle embedded within a NC matrix of ca. 1.71 nm in thickness and the elemental composition is confirmed in the corresponding STEM elemental mapping analysis (Fig. 6$b_1$–$b_4$). The OER performance was evaluated in 1.0 M KOH, and the results (Fig. 6c) show that within the context of $E_{10}$, most of the prepared samples exhibited a better activity than commercial $RuO_2$, and FeCoNi-2 (prepared at the initial feed ratio of Fe:Co:Ni = 3:4:3) stood out as the best among the series. For HER, the performance varied in the order of Pt > FeCo > FeCoNi-1 (Fe:Co:Ni = 4:4:2) > FeCoNi-2 > FeCoNi-3 (Fe:Co:Ni = 2:4:4) > CoNi > FeNi > Co (Fig. 6d). This suggests that the OER and HER activity can be readily adjusted by the elemental compositions of the metal alloy cores. DFT calculations based on a 55-atom metal cluster (Fig. 6e) show that (i) $\Delta G_{H^*}$ followed the same order as the experimental results, where the best catalyst FeCo exhibited the lowest $\Delta G_{H^*}$ (Fig. 6f), (ii) the calculated volcano plot (Fig. 6g) of OER suggested that the OER activity could be improved by incorporating multiple metals into the core and increasing the degrees of freedom of the alloys. Fig. 6h depicts the Bader charge transfer profiles of the various M@C structures, and the numbers of electron transfer were estimated to be 5.81, 6.69, 6.50 and 5.25 for M = Co, FeCo, FeCONi and CoNiFe, respectively. Therefore, one can see that the composition of the metal core can indeed efficiently affect the electronic structure of the graphene shell, a unique feature that can be exploited to tailor the catalytic activity towards different reactions.

## 4. Carbon shell effect

For M@C catalysts, reactions occur on the carbon shell surface. Thus, one can envisage that the electrocatalytic performance can also be readily manipulated by the structure of the carbon shell. One effective strategy is to dope the carbon materials with select heteroatoms [122–125]. Notably, for undoped carbon, the electrocatalytic performance is generally subpar [81,85,92,103,109,115,126]. For instance, in ORR, the onset potential ($E_{onset}$) of Co nanoparticles encapsulated in undoped carbon (Co@C) was 50 mV more negative than that of Pt/C; yet when the carbon was doped with nitrogen, the performance was actually better than that of Pt/C [88,92,101]. In some other studies [85,93,94,119], the performance of overall water splitting by Ni@C was found to be markedly

enhanced with a doped carbon shell, as compared to that with undoped carbon. In fact, experimentally, a wide range of dopants, including nonmetal elements and metal elements (Tables 1 and 2) have been incorporated into the C shell. For instance, the Ye group [39] prepared Co@C for HER electrocatalysis, where the carbon shell was doped by N alone or co-doped by N and B. Fig. 7a depicts the polarization curves of a series of Co@C electrocatalysts, from which the $\eta_{10}$ values can be identified at −284, −191, and −96 mV for Co@C, Co@NC and Co@BNC, respectively, suggesting that doping of the carbon shell indeed enhanced the HER activity, and the enhancement was more pronounced with dual doping than with mono-doping. To unravel the mechanistic origin, DFT calculations were carried out by using a $Co_{55}@C_{240}$ model, where a select number of C atoms were replaced by N and/or B. The $\Delta G_{H^*}$ results are plotted in Fig. 7b. One can see that the undoped carbon shell shows a very positive $\Delta G_{H^*}$, indicative of difficult H* adsorption, while the $\Delta G_{H^*}$ of the metal core is very negative, suggesting strong proton adsorption. Again, the formation of M@C composites led to a markedly reduced $\Delta G_{H^*}$ to 0.35 eV [57]. Interestingly, doping led to a further decrease of the $\Delta G_{H^*}$ to 0.23 eV for the $C_{234}N_6$ shell and even lower to 0.118 eV for the $C_{232}N_6B_2$ shell. This is contributed to charge transfer from the metal core to carbon shell and more importantly the introduction of an asymmetrical spin and charge density by doping of N and B due to their electronegativity difference, leading to the formation of more C and N as active sites for HER (Fig. 7c). In another study [89], Fe nanoparticles were encapsulated in N-doped Pod-like carbon nanotubes (Pod(N)−Fe) and used as ORR electrocatalysts. The resultant Pod(N)−Fe or Pod(N)−FeCo exhibited enhanced ORR activity, as compared to Pod-Fe with

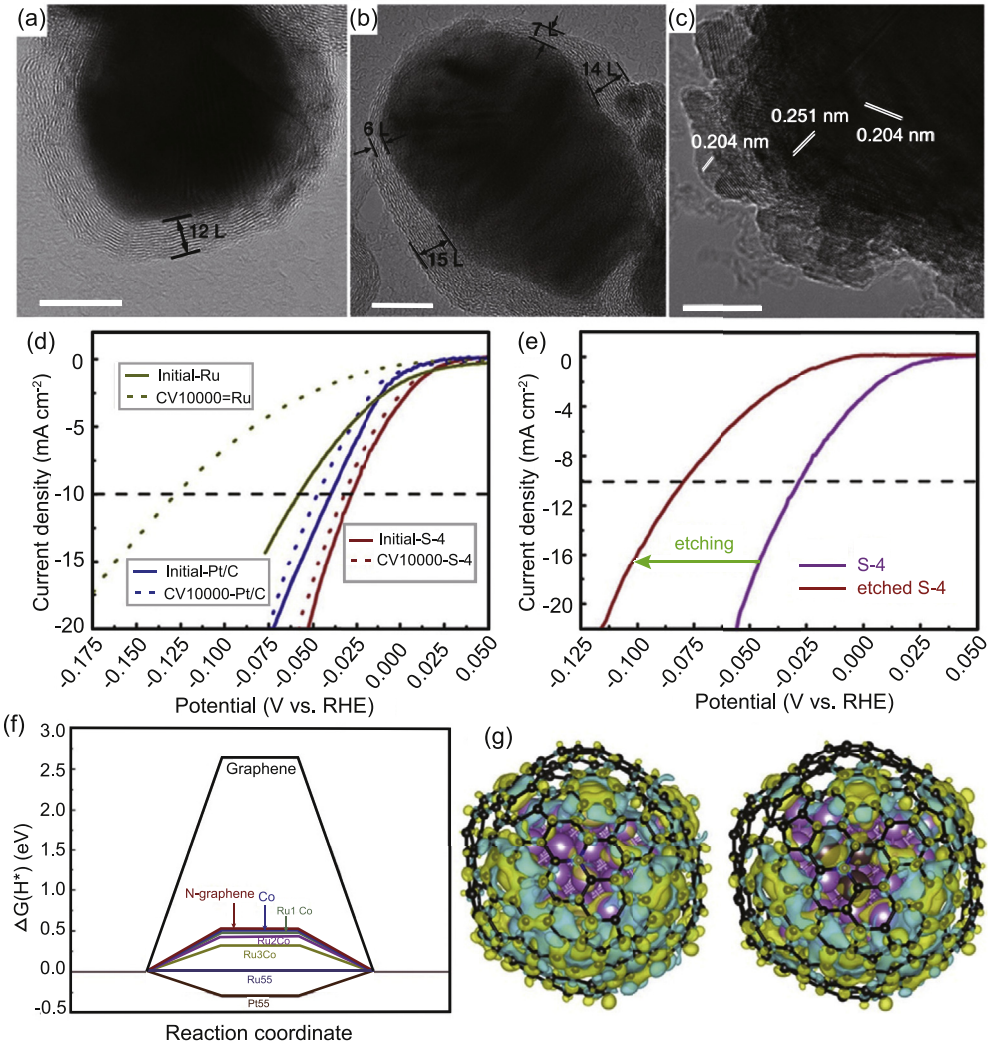


Fig. 5. (a–c) HRTEM images of RuCo@NG catalyst. Scale bar 10 nm. (d) Polarization curves of HER catalyzed by RuCo@NG (labeled "S-4"), Ru nanoparticles, and Pt/C in 1 M KOH in the first and 10,000th potential cycles. (e) Effect of 1 M HCl etching on the HER catalytic performance of RuCo@NC. (f) DFT calculated HER free energy diagram. (g) DFT calculated charge-density differences of $Co_{55}@N_1C_{239}$ and $Ru_3Co_{52}@N_1C_{239}$ models. The isosurface value of the color region is 0.01 e $A^{-3}$. The yellow and cyan regions refer to increased and decreased charge distributions, respectively (Reproduced with permission from Ref. [45] ©2017 The Authors).

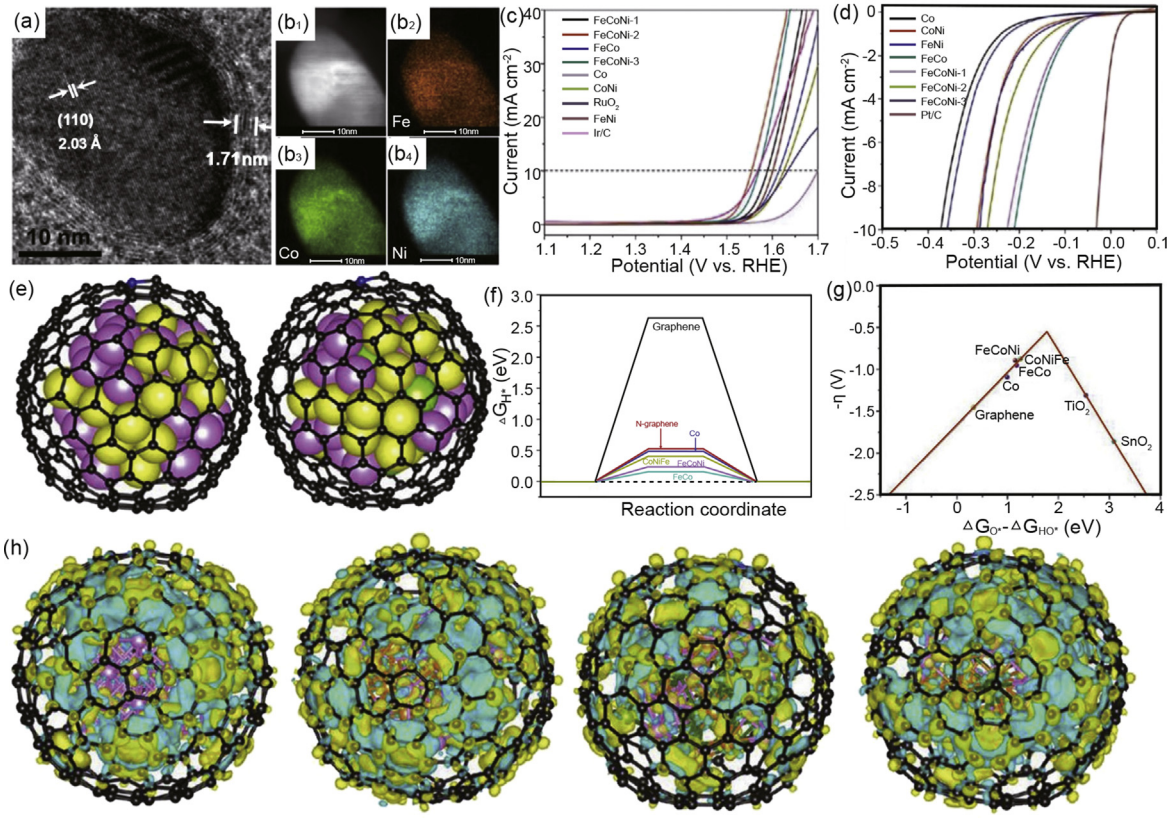


Fig. 6. (a) Representative TEM image of FeCoNi@NC. (b) STEM images of a single FeCoNi alloy nanoparticle and the corresponding elemental maps of Fe, Co, and Ni. (c) OER and (d) HER polarization curves of various M@NC catalysts in 1.0 M KOH. (e) Schematic models of M@NG hybrids. Left: FeCo@NG; Right: FeCoNi@NG, and the corresponding $\Delta G_{H^*}$ is shown in panel (f), whereas the calculated overpotential of OER versus ($\Delta G(O^*)-\Delta G(HO^*)$) is plotted in panel (g). (h) Calculated charge density difference of various M@C models (the core structures from left to right are Co, FeCo, $Fe_{24}Co_{24}Ni_7$, and $Fe_{15}Co_{20}Ni_{20}$, respectively). The isosurface value is 0.01 e $A^{-3}$, and yellow and cyan regions represented the increase and decrease of charge distributions, respectively (Reproduced with permission from Ref. [107] ©2016 American Chemical Society).

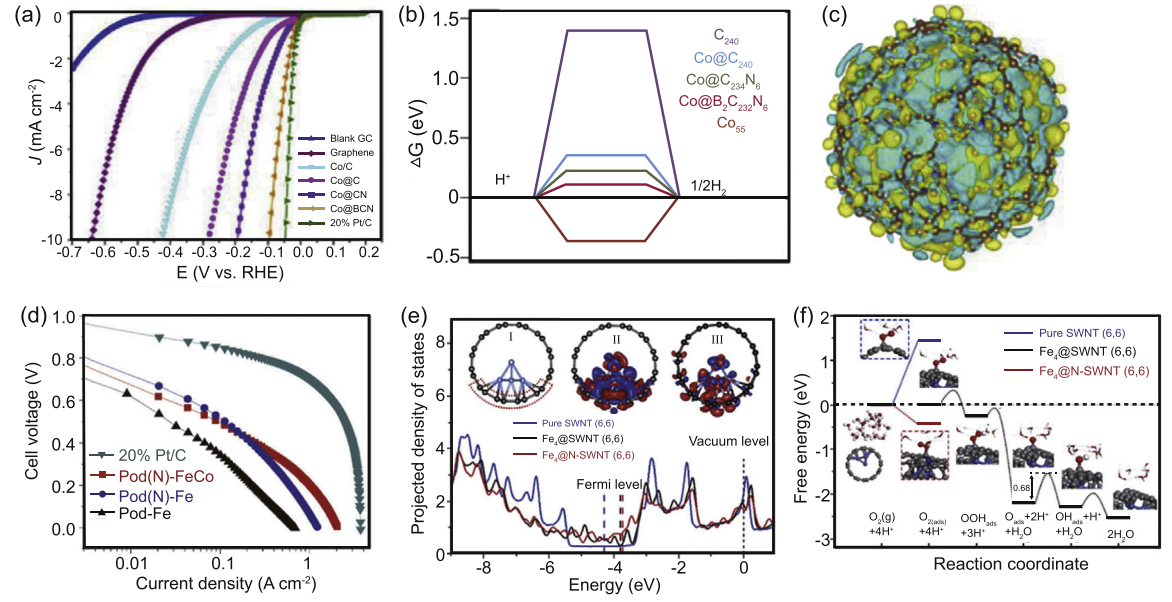


Fig. 7. (a) HER polarization curves of a series of M@C catalysts in 0.5 M $H_2SO_4$. (b) DFT calculated $\Delta G_{H^*}$ on different HER electrocatalysts. (c) Charge density difference of the $Co_{55}@C_{232}N_6B_2$ model. The isovalue is 0.0006 e $A^{-3}$. Yellow and cyan are charge accumulation and depletion with respect to an isolated $Co_{55}$ core and $C_{232}N_6B_2$ shell. (d) Single $H_2-O_2$ fuel cell performance tests with different cathode catalysts. (e) DFT calculated p-DOS of the p orbitals of C atoms in SWCNT or C atoms bonding to a $Fe_4$ cluster in $Fe_4$@SWCNT and $Fe_4$@N–SWCNT. Inset: I and II are the relaxed structures of $Fe_4$@SWCNT and the corresponding charge density difference; III is the charge density difference of $Fe_4$@N–SWCNT. The red and blue regions represent charge accumulation and depletion, respectively. (f) ORR free energy diagrams on various electrocatalysts (a–c: Reproduced with permission from Ref. [39] ©2015 American Chemical Society. d–f: Reproduced with permission from Ref. [89] ©2013 Wiley-VCH).

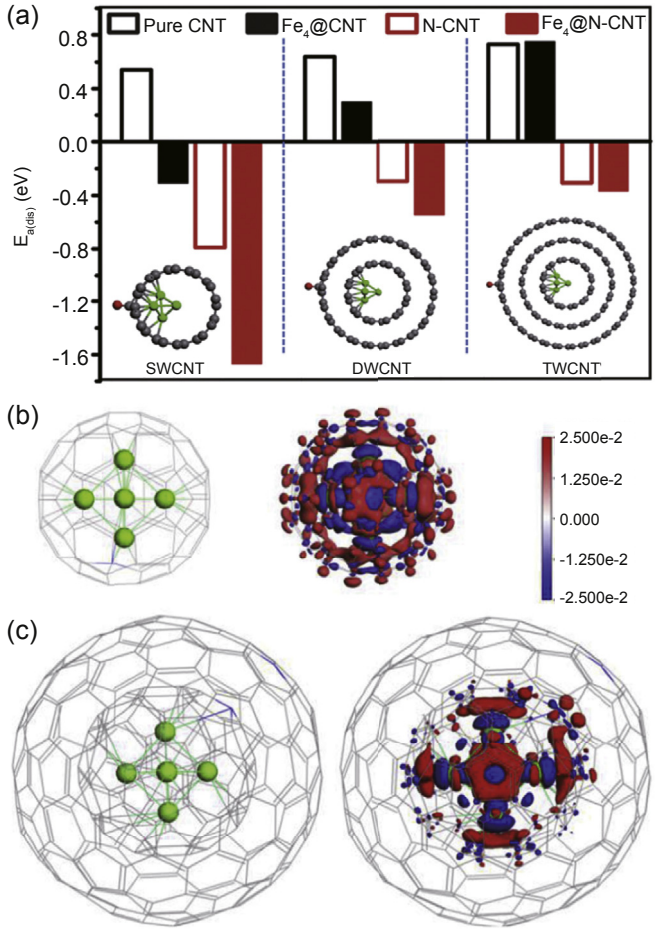


Fig. 8. (a) Dissociative adsorption energy of oxygen on the surface of various ORR catalyst models including CNT, N–CNT, $Fe_4$@CNT and $Fe_4$@N–CNT, where the number of CNT layer varies from 1 to 3. Models of Cu@NC with (b) 1 NC layer or (c) 2 NC layers, and the corresponding charge density differences. The red and blue regions represent the charge accumulation and depletion, respectively (a: Reproduced with permission from Ref. [127] ©2013 Royal Society of Chemistry; b–c: Reproduced with permission from Ref. [84] ©2017 American Chemical Society).

undoped CNT (Fig. 7d). DFT calculations using the models of $Fe_4$@SWCNT and $Fe_4$@N–SWCNT (Fig. 7e) show that based on the p-DOS of the p-orbital of $Fe_4$-bonded C and the charge density difference, N-doping increased the DOS near the Fermi level and reduced the work function of the surrounding area, as compared to that without N-doping. Fig. 7f displays the corresponding ORR free energy diagrams. One can see that after N-doping, the oxygen adsorption free energy decreased to −0.4 eV from +0.03 eV without N-doping, indicating that N-doping efficiently facilitated oxygen adsorption and the associative pathway to convert $O_2$ to $H_2O$. Overall, results from these studies demonstrate that dopants in the carbon shell have two major effects: to further manipulate the electronic structure of the surrounding atoms by charge transfer interactions; and to promote the formation of additional active sites.

The electrocatalytic activity of M@C also depends on the thickness of the carbon shell. For instance, the Bao group [127] carried out DFT calculations to study the effect of the number of CNT or N–CNT layers on the electrocatalytic activity of $Fe_4$@CNT and $Fe_4$@N–CNT. As shown in Fig. 8a, the dissociative adsorption energies of oxygen ($E_{a(dis)}$) increased almost linearly with the number of CNT layers increased from 1 to 3 for both $Fe_4$@CNT and $Fe_4$@N–CNT. Note that a smaller $E_{a(dis)}$ is expected for better ORR catalysts. In addition, the difference of the catalytic performance between CNT and $Fe_4$@CNT or between N–CNT and $Fe_4$@N–CNT diminished with the increase of the carbon nanotube layers, and the difference almost vanished when the number of nanotube layer reached 3, indicating that the effect of the metal cores now became negligible and the catalysts behaved equivalently to metal-free carbon alone [122–125]. In another study with Cu@NC [84], DFT calculations showed that charge transfer occurred from the Cu cores to the single layer NC shell, leading to manipulation of the adsorption energy of $O_2$ on the NC shell (Fig. 8b). However, for a shell of 2 NC layers (Fig. 8c), the electronic interactions were mainly between Cu core and the internal NC shell but not the external one. This apparently contradicts the experimental results described above. One possible reason is that in experimental study, the prepared M@C composites actually entail a range of carbon shell thicknesses; yet it is technically challenging to resolve a single carbon layer on metal nanoparticle surface that makes dominant contributions to the electrocatalytic activity.

The impacts of the thickness of the carbon shell have also been observed in HER electrocatalysis. For instance, Deng et al. [60] compared the HER activity of NiCo@NC for HER with CoNi nanoalloys of 4–7 nm in diameter encapsulated in a NC shell varied from 1 to 3 graphene layers by controlled pyrolysis at different temperatures (Fig. 9a–b). HER polarization curves (Fig. 9c) showed that the CoNi@NC prepared at 475 °C possessed the best HER catalytic activity among the series of samples except for Pt/C. Fig. 9d plots the $\Delta G_{H^*}$ difference between CoNi@NC and NC ($\Delta\Delta G_{H^*}$) and the electronic potentials from DFT calculations as a function of the number of NC layers. It can be clearly seen that with an increasing number of the NC layers from 1 to 3, the $\Delta\Delta G_{H^*}$ decreased from 0.8 eV to 0.1 eV while the electronic potential decreased from −0.5 eV to 0 eV, suggesting that an increase of the NC layer thickness diminished the effect of the CoNi cores on the HER activity, and when the thickness was equal to or greater than 3 layers, there was virtually no effect. The charge density difference profiles of CoNi@NC with 1–3 NC layers (Fig. 9e) also suggest that whereas electron transfer occurred from the CoNi core to the NC layers, it decreased dramatically with the NC layer thickness.

These studies clearly demonstrate that the number of graphene layers exhibits significant impacts on the electronic structure of the M@C nanostructures. Yet charge transfer from the metal cores to the carbon shell is primarily confined to the first three graphene layers. In most prior experimental studies, the M@C catalysts primarily entail a much thicker carbon shell. This suggests that one should be critical in developing a relevant structural model for theoretical simulations and calculations, such that the theoretical insights may be directly

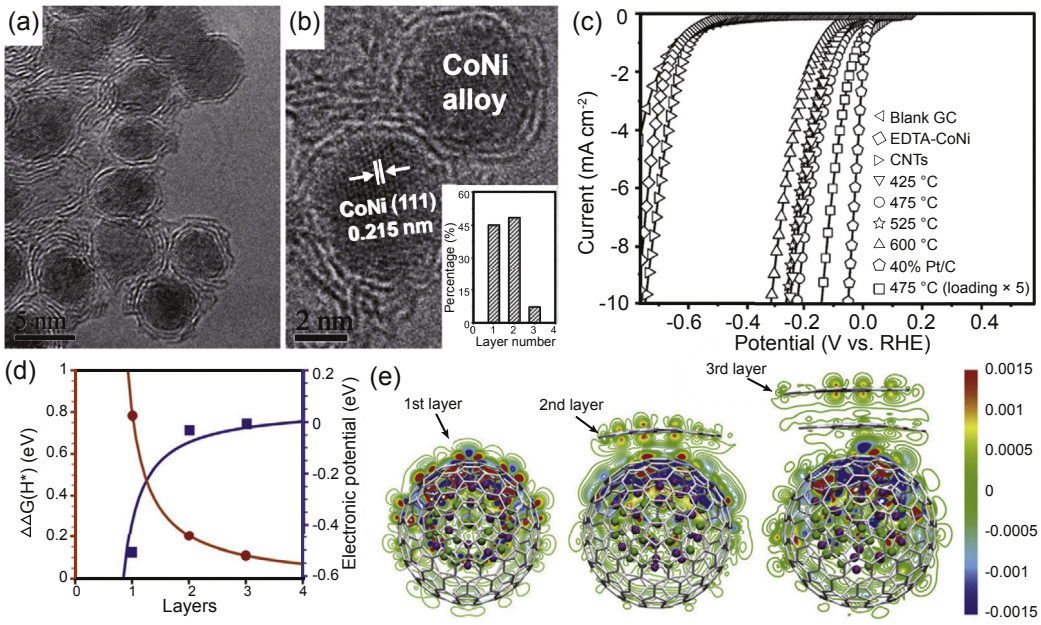


Fig. 9. (a–b) TEM and HRTEM images of CoNi@NC. Inset to (b) is the histogram of the number of NC layers. (c) HER polarization curves of a series of electrocatalysts measured in 0.5 M $H_2SO_4$. (d) $\Delta G_{H^*}$ difference between CoNi@NC and the NC shell ($\Delta\Delta G_{H^*}$) and electronic potential vs. the number of NC layers. (e) Charge density difference of CoNi@NC with 1–3 NC layers. The red and blue regions represent charge accumulation and depletion, respectively (Reproduced with permission from Ref. [60] ©2015 Wiley-VCH).

correlated with the experimental data to account for the electrocatalytic performance and, more importantly, to unravel the mechanistic origin. Meanwhile, it is highly desired to develop effective synthetic protocols for ready control of the carbon shell thickness, in which some progress has been made [35,128].

## 5. Third component effect

The electrocatalytic performance of M@C nanostructures can also be manipulated by a third component that is typically incorporated as part of the core or shell, or hybridized with the M@C composites. Such third components typically entails metal oxides, such as $TiO_2$ [129], CoO [61,130], $Co_3O_4$ [91,98,131] and $MM'O_x$ (M, M′ = Fe, Co, Ni, and Cu) [132–134], and can be used as multifunctional electrocatalysts towards ORR, OER and HER. For instance, the Sun group [132] prepared $CuCo/CuCoO_x$@NC hybrids as bifunctional electrocatalysts for overall water splitting, where a cell voltage ($E_{10ws}$) of only 1.53 V was needed to reach a 10 mA $cm^{-2}$ current density, and claimed that one of the contributions was from the metal–semiconductor Mott–Schottky structure which

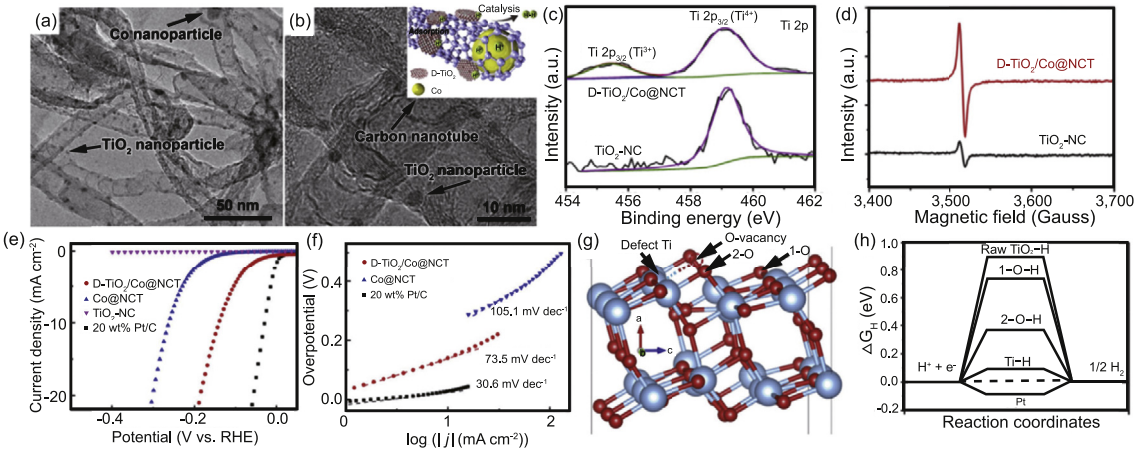


Fig. 10. (a–b) TEM images of D–$TiO_2$/Co@NCNT. Inset to (b) is a structural schematic. (c) XPS and (d) EPR spectra of Ti 2p in D–$TiO_2$/Co@NCNT and $TiO_2$–NC. (e) HER polarization curves of different electrocatalysts in 0.5 M $H_2SO_4$ electrolyte, and (f) the corresponding Tafel plots. (g) Atomic model of $TiO_2$ with one O vacancy after relaxation. (h) Calculated $\Delta G_{H^*}$ at different sites in the model (Reproduced with permission from Ref. [129] ©2017 Tsinghua University Press and Springer-Verlag Berlin Heidelberg).

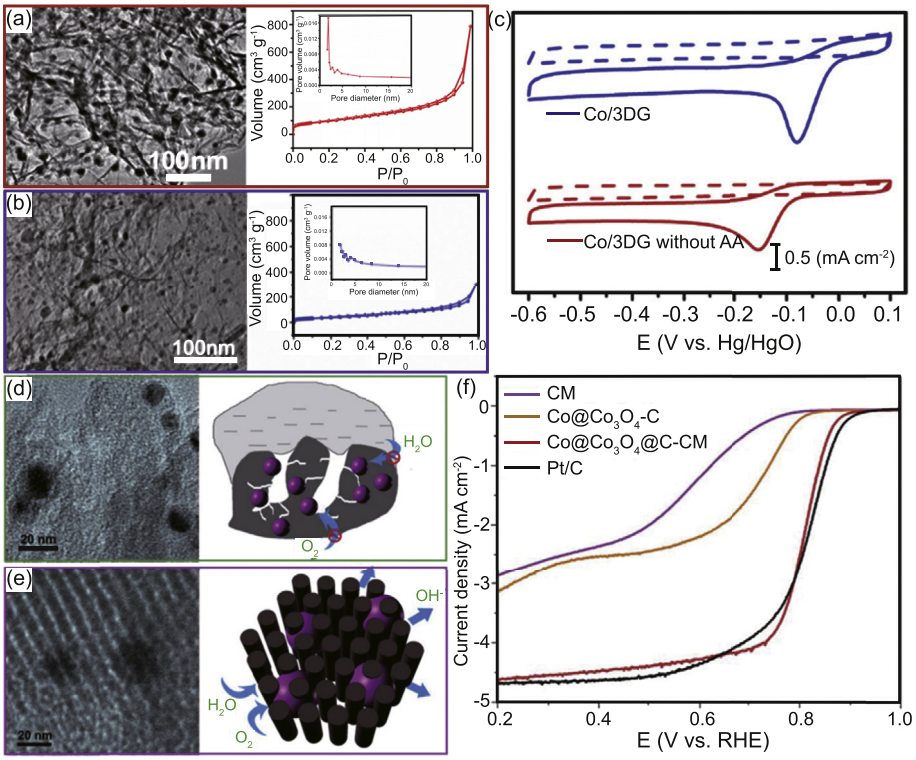


Fig. 11. (a–b) TEM image of Co@3DG (a) with and (b) without ascorbic acid treatment, and the corresponding $N_2$ adsorption–desorption isotherms and pore size distributions (insets). (c) CV curves of the electrocatalysts recorded in $N_2$ and $O_2$ saturated 0.1 M KOH. (d–e) TEM images of (d) disordered and (e) ordered Co@$Co_3O_4$@C, and the corresponding mass transport pathways during ORR. (f) ORR polarization curves of the various catalysts in 0.1 M KOH (a–c: Reproduced with permission from Ref. [92] ©2017, Springer-Verlag GmbH Germany; d–f: Reproduced with permission from Ref. [150] ©2015 The Royal Society of Chemistry).

optimized charge transfer in the material [135,136]. Jin et al. [130] prepared Co/$CoO_x$@NC as HER and OER bifunctional catalysts and found that the presence of $Co^{2+}$ enhanced the OER performance via a synergetic interaction between the cobalt metal and cobalt oxides. In another study, Yu et al. [129] examined the HER activity of Co@NCNT, and found that hybridization with defective $TiO_2$ (D–$TiO_2$/Co@NCNT) led to marked enhancement of the HER performance. The structure of the D–$TiO_2$/Co@NCNT hybrid was first characterized by TEM measurements (Fig. 10a–b), and the structural defects of $TiO_2$ were confirmed by XPS measurements where a $Ti^{3+}$ peak was identified at 455.2 eV (Fig. 10c), and EPR measurements showed a stronger radical $O^{2-}$ signal at g = 2.00 in D–$TiO_2$/Co@NCNT than in $TiO_2$–NC (Fig. 10d). Impressively, the resulting D–$TiO_2$/Co@NCNT composite exhibited an excellent HER activity with a low $\eta_{10}$ of −167 mV (Fig. 10e) and a small Tafel slope of 73.5 mV/dec (Fig. 10f). DFT calculations based on a relaxed model of defective $TiO_2$ with one O vacancy (Fig. 10g) showed that $\Delta G_{H^*}$ at the Ti defect site was only 0.081 eV, comparable to that of state-of-the-art catalysts Pt/C ($\Delta G_{H^*} = -0.09$ eV), indicating that the D–$TiO_2$ provided additional active sites for HER.

In another study [137], the Chen group prepared Fe/$Fe_3C$@NC nanorods, where the cores were Fe/$Fe_3C$ composite rods and the shells were N-doped graphene, and observed improved ORR activity in neutral electrolytes, as compared to commercial Pt/C. They then successfully used Fe/$Fe_3C$@NC as cathode catalysts for microbial fuel cells. In a further study [138], they developed a more complex structure consisting of Fe/$Fe_3C$@C nanoboxes on reduced graphene oxide (rGO), which exhibited apparent ORR activity in alkaline electrolyte. More recently, Wang et al. [139] synthesized Fe/$Fe_3C$ nanoparticles encapsulated in a N-doped graphene–CNT framework, which exhibited bifunctional activity towards both ORR and OER, and thus was used as oxygen electrodes in rechargeable Zn-air batteries. However, the role of $Fe_3C$ in the structures remained unknown, since no control experiments were included to examine and compare the activity of Fe@NC [89,140].

Separately, the Lou group [91] embedded Co nanoparticles within a carbon matrix and encapsulated the composites with a $Co_9S_8$ shell. They found the $Co_9S_8$ layer led to the generation of an increasing number of ORR active sites and hence enhanced ORR performance, as compared to that without the overlayer [83,88,91,92,99,102,141]. A variety of composite catalysts were prepared in a similar fashion, such as $Fe_3O_4$/$Co_9S_8$/rGO, Co/$Co_9S_8$/C, and Co/$Co_9S_8$/SN–C [142–144]. For instance, Hao et al. [145] embedded Co/CoP in N-doped carbon as tri-functional electrocatalysts for ORR, OER and HER, a unique feature for applications like water splitting and rechargeable metal-air battery. This is due to the addition of

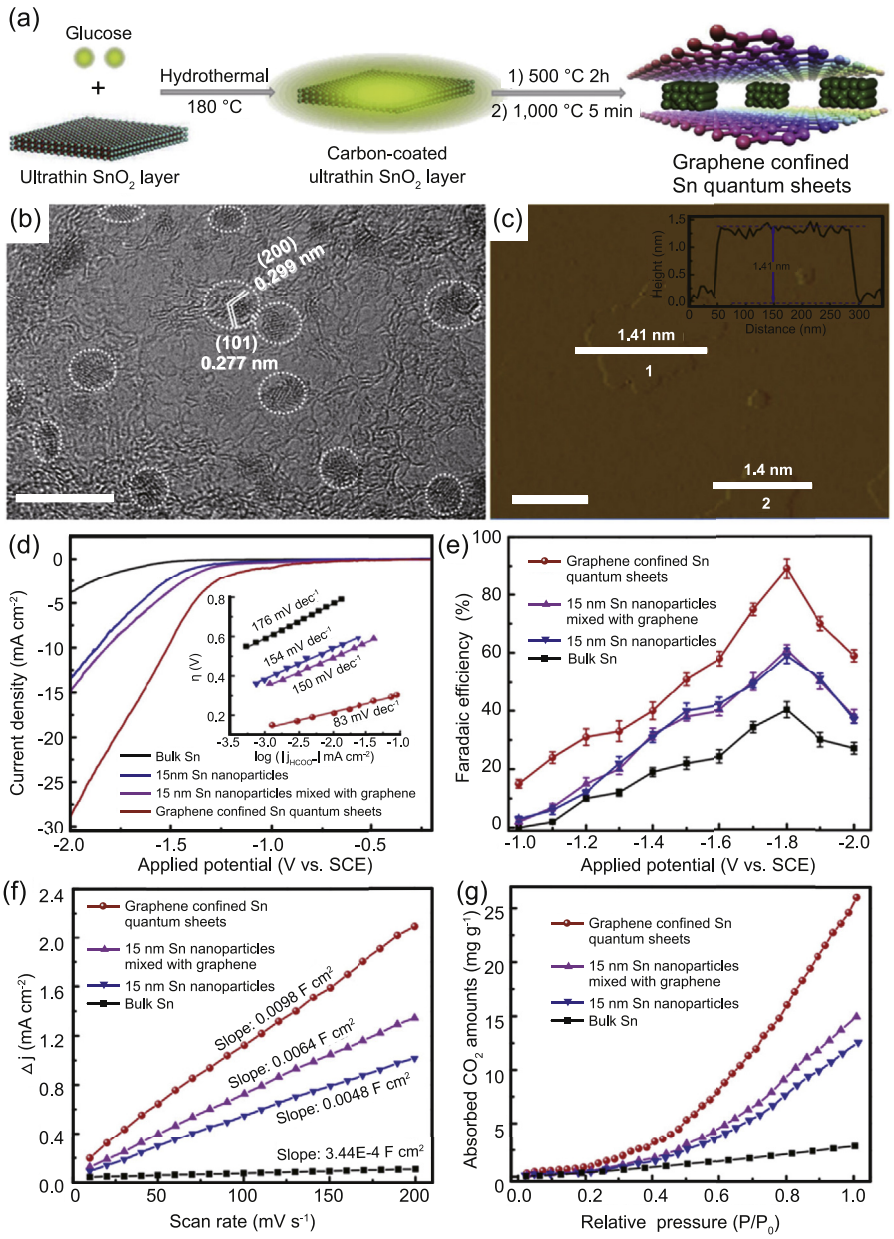


Fig. 12. (a) Schematic illustration for the synthesis of SnQD@G. (b) HRTEM image and (c) AFM image of SnQD@G. (d) LSV curves recorded in 0.1 M $NaHCO_3$ aqueous electrolyte with various $CO_2$RR catalysts, and (e) the corresponding Faradaic efficiency for formate production under different overpotentials. (f) Double-layer capacity derived from the plot of voltammetric current density versus scan rates. (g) $CO_2$ adsorption isotherms (Reproduced with permission from Ref. [103] ©2017 The Authors).

CoP that led to the formation of more active sites [146–148]. Furthermore, Jin et al. [149] prepared Co@C/$Co(OH)_2$ composites for HER electrocatalysis, where $Co(OH)_2$ was in-situ formed by an electrochemical treatment.

These representative examples highlight the unique strategies in the design and engineering of high-performance (multi-functional) catalysts by the incorporation of a third component, due to the following advantages: (i) generation of additional catalytic active sites, (ii) further control of the electronic properties of the M@C nanostructures due to synergetic interactions between the third component and M@C, and (iii) applications as multi-functional catalysts.

## 6. Morphology effect

In catalyst design, morphology is another important factor that needs to be taken into consideration besides the structural parameters discussed above. For instance, Chen et al. [92] encapsulated Co nanoparticles within 3D graphene (Co@3DG), and found that after ascorbic acid treatment, the sample exhibited enhanced ORR activity. From the TEM images in Fig. 11a–b, one can clearly see that ascorbic acid treatment did not change the 3D structures with Co nanoparticle wrapped inside except that more graphene wrinkles were formed. From the corresponding nitrogen adsorption–

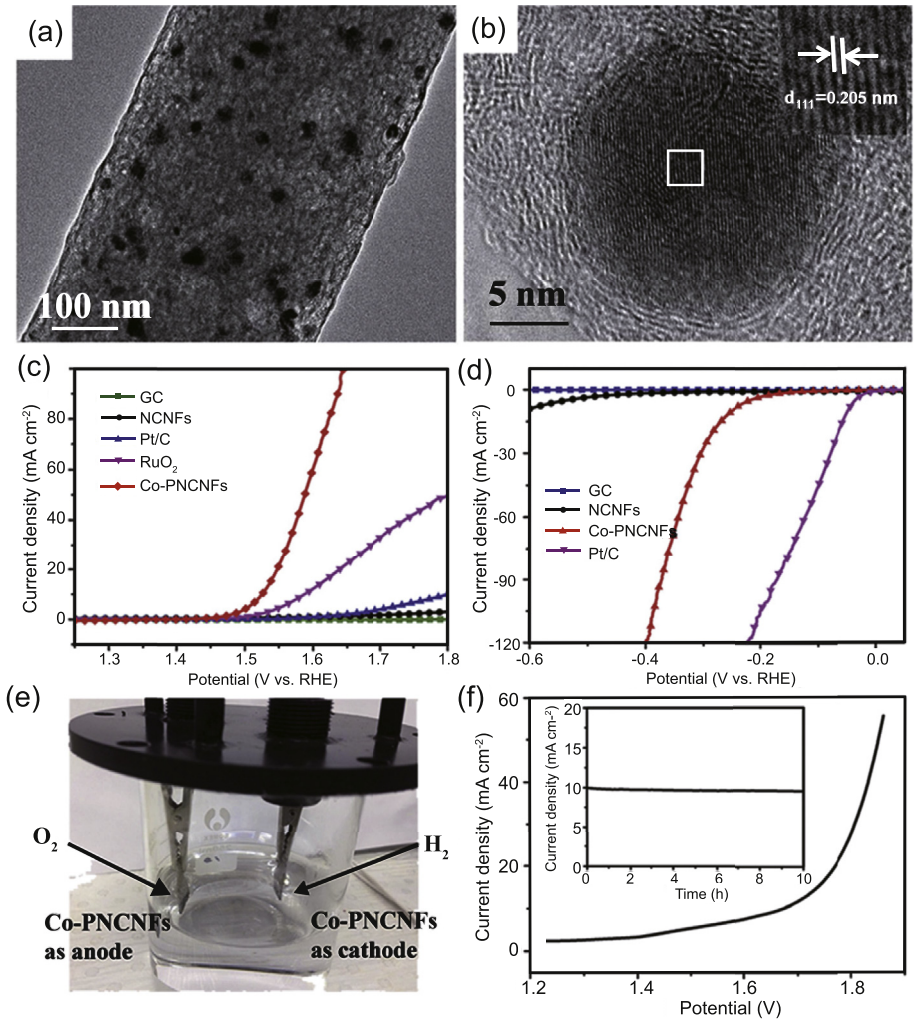


Fig. 13. (a–b) TEM images of a single carbon fiber with embedded Co nanoparticles (Co-PNCFs). (c) OER and (d) HER polarization curves of Co-PNCFs in 1.0 M KOH, in comparison with other catalysts. (e) Photograph of a water splitting cell using Co-PNCNFs as both anode and cathode catalysts, and (f) the corresponding LSV curve. Inset to (f) is the stability test at the potential of 1.66 V over 10 h (Reproduced with permission from Ref. [94] ©2016 The Royal Society of Chemistry).

desorption isotherms, the BET surface area of Co@3DG was found to be markedly enhanced after acid treatment (ca. 348 $m^2\ g^{-1}$), due to the generation of an increasing number of mesopores and macropores. In cyclic voltammetric measurements, after acid treatment, Co@3DG possessed a more positive ORR peak potential at −0.08 V (vs. Hg/HgO) and higher cathodic current density of 2.25 mA $cm^{-2}$ than the one without acid treatment (ORR peak potential −0.15 V, and peak current density 1.5 mA $cm^{-2}$) in 0.1 M KOH electrolyte (Fig. 11c). In another study [150], the Guo group studied and compared the ORR activity of Co@$Co_3O_4$@C, where the carbon shell was either a highly ordered porous carbon matrix or disordered porous carbon matrix (Fig. 11d–e). Interestingly, the ordered sample (Co@$Co_3O_4$@C–CM) showed a much higher ORR activity ($E_{onset}$ = +0.93 V and $E_{½}$ = +0.81 V) than the disordered counterpart (Co@$Co_3O_4$–C, $E_{onset}$ = +0.85 V and $E_{½}$ = +0.70 V). In fact, the ORR performance of the former is close to that of Pt/C in $O_2$-saturated 0.1 M KOH (Fig. 11f). This is accounted for by the fact that the ordered open space could better facilitate rapid mass transfer of the gas and electrolyte, which was further confirmed by studies with other catalysts [151,152]. Indeed, the morphology of the M@C composites can have significant effects on both the electron transfer and mass transport dynamics of the catalytic reactions, and thus is an important factor in catalyst design and engineering [153–156].

## 7. Applications

In addition to HER, OER and ORR, M@C nanocomposites have also shown potential applications towards other important reactions such as $CO_2$RR. For instance, the Xie group [103] synthesized graphene confined Sn quantum dots (SnQD@G) using a two-step approach (Fig. 12a). HRTEM measurements (Fig. 12b) suggested that the SnQD was wrapped and well dispersed in the graphene matrix, and AFM study (Fig. 12c) showed that the SnQD exhibited a 2D sheet-like feature with a thickness of ca. 1.41 nm. Interestingly, the SnQD@G sample exhibited a higher catalytic activity towards $CO_2$RR in $CO_2$-saturated 0.1 M $NaHCO_3$ than Sn nanoparticles, bulk Sn or the mixture of Sn nanoparticles and graphene (Fig. 12d). Fig. 12e depicts the $CO_2$ reduction

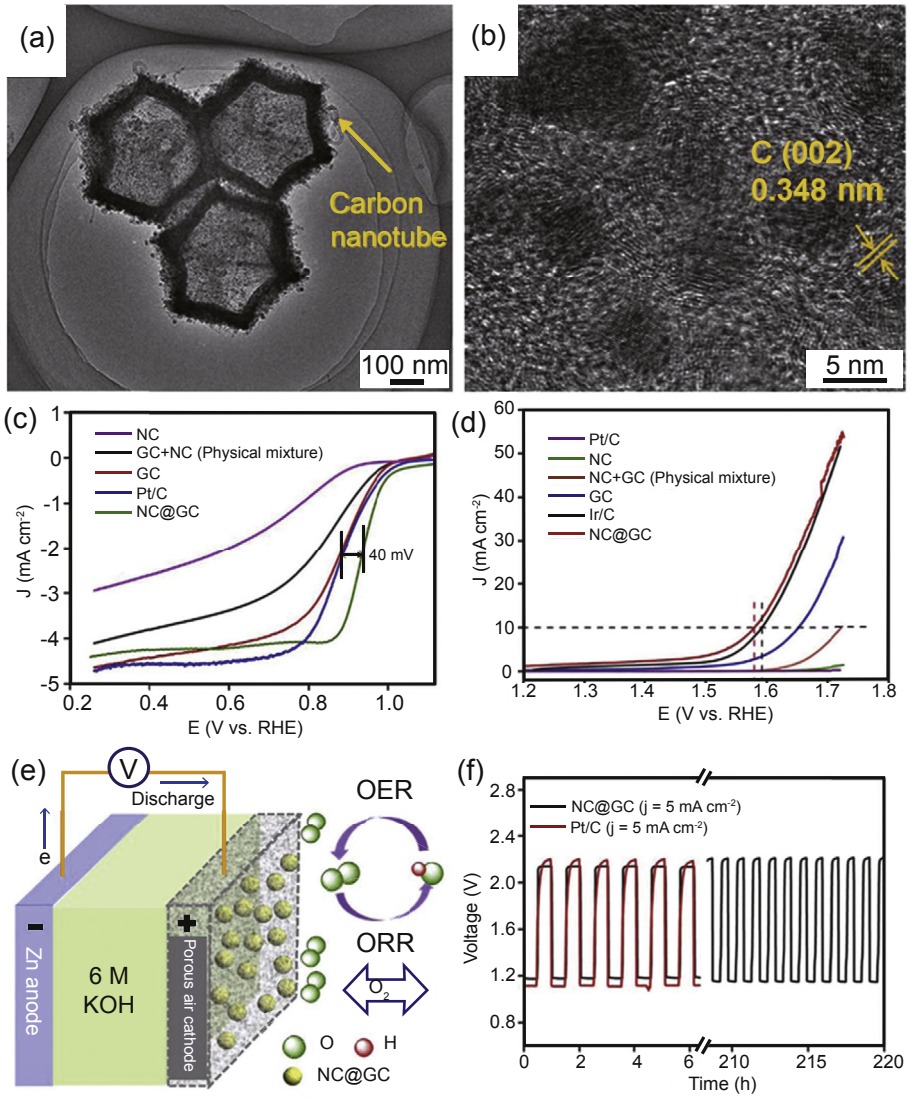


Fig. 14. (a–b) TEM images of Co@NC@GC. Polarization curves of various electrocatalysts for (c) ORR and (d) OER in 0.1 M KOH. (e) Schematic of a rechargeable Zn-air battery. (f) Cycling performance of a Zn-air battery using Co@NC@GC or Pt/C as electrocatalysts at 5 mA $cm^{-2}$ (Reproduced with permission from Ref. [101] ©2016 Elsevier).

products at various overpotential and the SnQD@G sample showed a higher faradaic efficiency for formate production than other catalysts in the series, which reached a maximum at −1.8 V. This may be due to the high electrochemical surface area of SnQD@G, as manifested in the double-layer capacitance (Fig. 12f). Consistently, the $CO_2$ adsorption capacity of the SnQD@G catalyst reached 26.1 mg/g at 1 atm, which was 9, 2 and 1.75 times that of bulk Sn, Sn nanoparticles and mixture of Sn nanoparticles and graphene, respectively, as shown in Fig. 12g.

Additionally, one of the advantages of M@C nanocomposites is the multi-functional activity that is critical in the applications of, for instance, overall water splitting [13–15] which requires the electrocatalysts to be active for both OER and HER and rechargeable metal-air batteries [16–18] where active electrocatalysts are needed for both ORR and OER. Here we highlight the applications of two M@C catalysts in these electrochemical devices, with additional examples listed in Tables 1 and 2. In one study, Zhao et al. [94] prepared Co nanoparticles embedded in porous N-doped carbon fibers (Co@NC, Fig. 13a–b), which exhibited apparent activity for both OER ($E_{10}$ = +1.515 V, Fig. 13c) and HER ($\eta_{10}$ = −0.249 V, Fig. 13d) in 1.0 M KOH. Using the Co@NC as both cathode and anode catalysts for overall water splitting in 1.0 M KOH, the authors observed an $E_{10ws}$ value of only 1.66 V, and there was almost no current loss after 10 h's continuous operation at this cell voltage (Fig. 13e–f). In another study [101], Wang et al. prepared Co@NC@GC hybrids (Fig. 14a–b). The sample showed bifunctional catalytic performance towards ORR and OER, with an ORR $E_{½}$ of +0.93 V, 40 mV more positive than that of commercial Pt/C, and OER $E_{10}$ of +1.57 V, as compared to that (+1.59 V) for Ir/C (Fig. 14c–d). That is, the overall potential for the oxygen electrode was only 0.64 V, which was much smaller than leading results in recent literatures [157–160]. With the unique bifunctional characteristics, the catalysts were used as

electrode materials for rechargeable Zn-air battery (Fig. 14e). Fig. 14f compares the battery performance with that using commercial Pt/C as electrode catalysts. One can see that Co@NC@GC needed ca. 0.95 V to drive a 5 mA/cm$^{-2}$ charge/discharge current density, which was lower than that of Pt/C (1.10 V).

## 8. Summary and perspectives

In summary, M@C core@shell nanocomposites have emerged as a new class of functional nanomaterials that may be exploited as high-performance electrocatalysts towards diverse reactions, due to charge transfer from the metal core to the carbon shell. This synergistic interaction can be readily manipulated by the chemical nature and structure of the metal core (elemental composition, core size, etc) as well as the carbon shell (doping and layer thickness). Further manipulation of the catalytic performance can be achieved by surface morphologies and integration of a third component into the composites, as manifested in a range of studies involving reactions such as ORR, OER, HER and $CO_2$RR.

In a number of studies that combine theoretical and experimental results, the structural models for theoretical simulations are generally oversimplified. This raises a significant question about the relevance between the two results. In particular, theoretical studies have shown that charge transfer from the metal cores to the carbon shell is primarily confined to the first graphene layer and diminishes sharply with increasing graphene layer thickness, and virtually no impacts are observed with a carbon shell of three or more graphene layers. By contrast, most experimental samples show a much thicker carbon shell. This is likely due to the dispersity of the carbon layer thickness in the samples, and it is a technical challenge to resolve carbon shells of only a few graphene layers. Therefore, a knowledge gap remains in the direct correlation between the experimental and theoretical results. Development of experimental protocols to prepare M@C with a well-defined number of graphene layers is highly desired.

Nevertheless, one can see that the electrocatalytic performance of M@C is apparent and should be of interest in a wide range of important applications, such as full water splitting and metal-air batteries, thanks to the multifunctional activity that can be readily tuned by the composite structures. Promising progress has indeed been made along this line. Continuing research is desired to further improve and eventually optimize the catalytic performance.

## Conflict of interest

The authors declare no conflict of interests.

## Acknowledgment

The authors thank the National Science Foundation (CHE-1710408) for partial support of the work.

## References

[1] M. Shao, Q. Chang, J.P. Dodelet, R. Chenitz, Chem. Rev. 116 (2016) 3594–3657.
[2] J. Wang, F. Xu, H. Jin, Y. Chen, Y. Wang, Adv. Mater. 29 (2017) 1605838.
[3] D.D. Zhu, J.L. Liu, S.Z. Qiao, Adv. Mater. 28 (2016) 3423–3452.
[4] J. Qiao, Y. Liu, F. Hong, J. Zhang, Chem. Soc. Rev. 43 (2014) 631–675.
[5] N.T. Suen, S.F. Hung, Q. Quan, N. Zhang, Y.J. Xu, H.M. Chen, Chem. Soc. Rev. 46 (2017) 337–365.
[6] M. Tahir, L. Pan, F. Idrees, X. Zhang, L. Wang, J.-J. Zou, Z.L. Wang, Nano Energy 37 (2017) 136–157.
[7] Z.W. Seh, J. Kibsgaard, C.F. Dickens, I. Chorkendorff, J.K. Norskov, T.F. Jaramillo, Science 355 (2017) eaad4998.
[8] C. Chen, Y. Kang, Z. Huo, Z. Zhu, W. Huang, H.L. Xin, J.D. Snyder, D. Li, J.A. Herron, M. Mavrikakis, M. Chi, K.L. More, Y. Li, N.M. Markovic, G.A. Somorjai, P. Yang, V.R. Stamenkovic, Science 343 (2014) 1339–1343.
[9] H. Over, Chem. Rev. 112 (2012) 3356–3426.
[10] C.C. McCrory, S. Jung, J.C. Peters, T.F. Jaramillo, J. Am. Chem. Soc. 135 (2013) 16977–16987.
[11] Y. Lee, J. Suntivich, K.J. May, E.E. Perry, Y. Shao-Horn, J. Phys. Chem. Lett. 3 (2012) 399–404.
[12] W. Sheng, H.A. Gasteiger, Y. Shao-Horn, J. Electrochem. Soc. 157 (2010) B1529.
[13] B. Xiong, L. Chen, J. Shi, ACS Catal. 8 (2018) 3688–3707.
[14] M.I. Jamesh, J. Power Sources 333 (2016) 213–236.
[15] Y. Wang, B. Kong, D. Zhao, H. Wang, C. Selomulya, Nano Today 15 (2017) 26–55.
[16] F. Cheng, J. Chen, Chem. Soc. Rev. 41 (2012) 2172–2192.
[17] D.U. Lee, P. Xu, Z.P. Cano, A.G. Kashkooli, M.G. Park, Z. Chen, J. Mater. Chem. A 4 (2016) 7107–7134.
[18] Z.L. Wang, D. Xu, J.J. Xu, X.B. Zhang, Chem. Soc. Rev. 43 (2014) 7746–7786.
[19] D.M. Alonso, S.G. Wettstein, J.A. Dumesic, Chem. Soc. Rev. 41 (2012) 8075–8098.
[20] Y.J. Wang, N.N. Zhao, B.Z. Fang, H. Li, X.T.T. Bi, H.J. Wang, Chem. Rev. 115 (2015) 3433–3467.
[21] C.H. Cui, S.H. Yu, Acc. Chem. Res. 46 (2013) 1427–1437.
[22] Z.W. Quan, Y.X. Wang, J.Y. Fang, Acc. Chem. Res. 46 (2013) 191–202.
[23] B.E. Hayden, Acc. Chem. Res. 46 (2013) 1858–1866.
[24] D.K. Perivoliotis, N. Tagmatarchis, Carbon 118 (2017) 493–510.
[25] N.S. Porter, H. Wu, Z.W. Quan, J.Y. Fang, Acc. Chem. Res. 46 (2013) 1867–1877.
[26] J.Y. Chen, B. Lim, E.P. Lee, Y.N. Xia, Nano Today 4 (2009) 81–95.
[27] T. Asefa, Acc. Chem. Res. 49 (2016) 1873–1883.
[28] Y.P. Zhu, C. Guo, Y. Zheng, S.Z. Qiao, Acc. Chem. Res. 50 (2017) 915–923.
[29] X. Zou, Y. Zhang, Chem. Soc. Rev. 44 (2015) 5148–5180.
[30] T. Wang, H. Xie, M. Chen, A. D'Aloia, J. Cho, G. Wu, Q. Li, Nano Energy 42 (2017) 69–89.
[31] Y. Peng, B. Lu, S. Chen, Adv. Mater. (2018), 1801995.
[32] G.H. Wang, J. Hilgert, F.H. Richter, F. Wang, H.J. Bongard, B. Spliethoff, C. Weidenthaler, F. Schuth, Nat. Mater. 13 (2014) 293–300.
[33] X. Pan, Z. Fan, W. Chen, Y. Ding, H. Luo, X. Bao, Nat. Mater. 6 (2007) 507–511.
[34] Z. Wen, J. Liu, J. Li, Adv. Mater. 20 (2008) 743–747.
[35] X. Cui, P. Ren, D. Deng, J. Deng, X. Bao, Energy Environ. Sci. 9 (2016) 123–129.
[36] H. Fei, Y. Yang, Z. Peng, G. Ruan, Q. Zhong, L. Li, E.L. Samuel, J.M. Tour, ACS Appl. Mater. Interfaces 7 (2015) 8083–8087.
[37] Q. Mo, N. Chen, M. Deng, L. Yang, Q. Gao, ACS Appl. Mater. Interfaces 9 (2017) 37721–37730.
[38] X. Dai, Z. Li, Y. Ma, M. Liu, K. Du, H. Su, H. Zhuo, L. Yu, H. Sun, X. Zhang, ACS Appl. Mater. Interfaces 8 (2016) 6439–6448.
[39] H. Zhang, Z. Ma, J. Duan, H. Liu, G. Liu, T. Wang, K. Chang, M. Li, L. Shi, X. Meng, K. Wu, J. Ye, ACS Nano 10 (2016) 684–694.

[40] X. Zou, X. Huang, A. Goswami, R. Silva, B.R. Sathe, E. Mikmekova, T. Asefa, Angew. Chem. Int. Ed. 53 (2014) 4372–4376.
[41] F. Lyu, Q. Wang, H. Zhu, M. Du, L. Wang, X. Zhang, Green Energy Environ. 2 (2017) 151–159.
[42] D. Hou, W. Zhou, K. Zhou, Y. Zhou, J. Zhong, L. Yang, J. Lu, G. Li, S. Chen, J. Mater. Chem. A 3 (2015) 15962–15968.
[43] Z. Zhang, S. Liu, X. Tian, J. Wang, P. Xu, F. Xiao, S. Wang, J. Mater. Chem. A 5 (2017) 10876–10884.
[44] J. Chen, G. Xia, P. Jiang, Y. Yang, R. Li, R. Shi, J. Su, Q. Chen, ACS Appl. Mater. Interfaces 8 (2016) 13378–13383.
[45] J. Su, Y. Yang, G. Xia, J. Chen, P. Jiang, Q. Chen, Nat. Commun. 8 (2017) 14969.
[46] P. Jiang, J. Chen, C. Wang, K. Yang, S. Gong, S. Liu, Z. Lin, M. Li, G. Xia, Y. Yang, J. Su, Q. Chen, Adv. Mater. 30 (2018), 1705324.
[47] Y. Zheng, Y. Jiao, L.H. Li, T. Xing, Y. Chen, M. Jaroniec, S.Z. Qiao, ACS Nano 8 (2014) 5290–5296.
[48] J.K. Norskov, T. Bligaard, J. Rossmeisl, C.H. Christensen, Nat. Chem. 1 (2009) 37–46.
[49] L. Yu, X. Pan, X. Cao, P. Hu, X. Bao, J. Catal. 282 (2011) 183–190.
[50] E. Skulason, G.S. Karlberg, J. Rossmeisl, T. Bligaard, J. Greeley, H. Jonsson, J.K. Norskov, Phys. Chem. Chem. Phys. 9 (2007) 3241–3250.
[51] L. Zhang, J. Niu, L. Dai, Z. Xia, Langmuir 28 (2012) 7542–7550.
[52] J.K. Nørskov, J. Rossmeisl, A. Logadottir, L.R. Lindqvist, J.R. Kitchin, T. Bligaard, H. Jonsson, J. Phys. Chem. B 108 (2004) 17886–17892.
[53] E. Skúlason, V. Tripkovic, M.E. Björketun, S. Gudmundsdóttir, G. Karlberg, J. Rossmeisl, T. Bligaard, H. Jónsson, J.K. Nørskov, J. Phys. Chem. C 114 (2010) 18182–18197.
[54] Y. Li, H. Wang, L. Xie, Y. Liang, G. Hong, H. Dai, J. Am. Chem. Soc. 133 (2011) 7296–7299.
[55] W. Zhou, J. Zhou, Y. Zhou, J. Lu, K. Zhou, L. Yang, Z. Tang, L. Li, S. Chen, Chem. Mater. 27 (2015) 2026–2032.
[56] R. Parsons, Trans. Faraday Soc. 54 (1958) 1053–1063.
[57] J.K. Nørskov, T. Bligaard, A. Logadottir, J.R. Kitchin, J.G. Chen, S. Pandelov, U. Stimming, J. Electrochem. Soc. 152 (2005) J23.
[58] J. Greeley, T.F. Jaramillo, J. Bonde, I.B. Chorkendorff, J.K. Norskov, Nat. Mater. 5 (2006) 909–913.
[59] Y. Zheng, Y. Jiao, Y. Zhu, L.H. Li, Y. Han, Y. Chen, A. Du, M. Jaroniec, S.Z. Qiao, Nat. Commun. 5 (2014) 3783.
[60] J. Deng, P. Ren, D. Deng, X. Bao, Angew. Chem. Int. Ed. 54 (2015) 2100–2104.
[61] W. Pei, S. Zhou, Y. Bai, J. Zhao, Carbon 133 (2018) 260–266.
[62] B. Hammer, J.K. Norskov, Nature 376 (1995) 238.
[63] J. Rossmeisl, Z.W. Qu, H. Zhu, G.J. Kroes, J.K. Nørskov, J. Electroanal. Chem. 607 (2007) 83–89.
[64] H. Dau, C. Limberg, T. Reier, M. Risch, S. Roggan, P. Strasser, ChemCatChem 2 (2010) 724–761.
[65] I.C. Man, H.-Y. Su, F. Calle-Vallejo, H.A. Hansen, J.I. Martínez, N.G. Inoglu, J. Kitchin, T.F. Jaramillo, J.K. Nørskov, J. Rossmeisl, ChemCatChem 3 (2011) 1159–1165.
[66] R.V. Mom, J. Cheng, M.T.M. Koper, M. Sprik, J. Phys. Chem. C 118 (2014) 4095–4102.
[67] P. Liao, J.A. Keith, E.A. Carter, J. Am. Chem. Soc. 134 (2012) 13296–13309.
[68] I.E. Stephens, A.S. Bondarenko, U. Grønbjerg, J. Rossmeisl, I. Chorkendorff, Energy Environ. Sci. 5 (2012) 6744–6762.
[69] F. Calle-Vallejo, M.T.M. Koper, Electrochim. Acta 84 (2012) 3–11.
[70] Y. Jiao, Y. Zheng, M. Jaroniec, S.Z. Qiao, J. Am. Chem. Soc. 136 (2014) 4394–4403.
[71] B. Lu, T.J. Smart, D. Qin, J.E. Lu, N. Wang, L. Chen, Y. Peng, Y. Ping, S. Chen, Chem. Mater. 29 (2017) 5617–5628.
[72] F. Calle-Vallejo, J.I. Martinez, J. Rossmeisl, Phys. Chem. Chem. Phys. 13 (2011) 15639–15643.
[73] I.C. Man, H.Y. Su, F. Calle-Vallejo, H.A. Hansen, J.I. Martínez, N.G. Inoglu, J. Kitchin, T.F. Jaramillo, J.K. Nørskov, J. Rossmeisl, ChemCatChem 3 (2011) 1156–1165.
[74] S. Trasatti, J. Electroanal. Chem. Interfacial Electrochem. 39 (1972) 163–184.
[75] N.D. Lang, W. Kohn, Phys. Rev. B 3 (1971) 1215–1223.
[76] F. Tao, M.E. Grass, Y. Zhang, D.R. Butcher, J.R. Renzas, Z. Liu, J.Y. Chung, B. Mun, M. Salmeron, G.A. Somorjai, Science 322 (2008) 932–934.
[77] Y. Xu, S. Yin, C. Li, K. Deng, H. Xue, X. Li, H. Wang, L. Wang, J. Mater. Chem. A 6 (2018) 1376–1381.
[78] Y. Xu, Y. Li, S. Yin, H. Yu, H. Xue, X. Li, H. Wang, L. Wang, Nanotechnology 29 (2018), 225403.
[79] V. Di Noto, E. Negro, S. Polizzi, F. Agresti, G.A. Giffin, ChemSusChem 5 (2012) 2451–2459.
[80] N. Du, C. Wang, R. Long, Y. Xiong, Nano Res. 10 (2017) 3228–3237.
[81] Q. Jin, B. Ren, D. Li, H. Cui, C. Wang, ACS Appl. Mater. Interfaces 9 (2017) 31913–31921.
[82] G. Zhang, P. Wang, W.T. Lu, C.Y. Wang, Y.K. Li, C. Ding, J. Gu, X.S. Zheng, F.F. Cao, ACS Appl. Mater. Interfaces 9 (2017) 28566–28576.
[83] Z. Wang, S. Xiao, Z. Zhu, X. Long, X. Zheng, X. Lu, S. Yang, ACS Appl. Mater. Interfaces 7 (2015) 4048–4055.
[84] H. Shao, X. Zhang, H. Huang, K. Zhang, M. Wang, C. Zhang, Y. Yang, M. Wen, W. Zheng, ACS Appl. Mater. Interfaces 9 (2017) 41945–41954.
[85] L. Ai, T. Tian, J. Jiang, ACS Sustain. Chem. Eng. 5 (2017) 4771–4777.
[86] Y. Hou, Z. Wen, S. Cui, S. Ci, S. Mao, J. Chen, Adv. Funct. Mater. 25 (2015) 872–882.
[87] M. Zeng, Y. Liu, F. Zhao, K. Nie, N. Han, X. Wang, W. Huang, X. Song, J. Zhong, Y. Li, Adv. Funct. Mater. 26 (2016) 4397–4404.
[88] Y.Z. Chen, C. Wang, Z.Y. Wu, Y. Xiong, Q. Xu, S.H. Yu, H.L. Jiang, Adv. Mater. 27 (2015) 5010–5016.
[89] D. Deng, L. Yu, X. Chen, G. Wang, L. Jin, X. Pan, J. Deng, G. Sun, X. Bao, Angew. Chem. Int. Ed. 52 (2013) 371–375.
[90] S. Zhang, X. Xiao, T. Lv, X. Lv, B. Liu, W. Wei, J. Liu, Appl. Surf. Sci. 446 (2018) 10–17.
[91] S. Zhang, Y. Zhang, W. Jiang, X. Liu, S. Xu, R. Huo, F. Zhang, J.-S. Hu, Carbon 107 (2016) 162–170.
[92] Z.-Y. Chen, Y.-N. Yu, S.-J. Bao, M.-Q. Wang, Y.-N. Li, M.-w. Xu, J Solid State Electr. 21 (2017) 3641–3648.
[93] F. Yang, P. Zhao, X. Hua, W. Luo, G. Cheng, W. Xing, S. Chen, J. Mater. Chem. A 4 (2016) 16057–16063.
[94] Y. Zhao, J. Zhang, K. Li, Z. Ao, C. Wang, H. Liu, K. Sun, G. Wang, J. Mater. Chem. A 4 (2016) 12818–12824.
[95] S.H. Noh, M.H. Seo, X. Ye, Y. Makinose, T. Okajima, N. Matsushita, B. Han, T. Ohsaka, J. Mater. Chem. A 3 (2015) 22031–22034.
[96] T. Wang, Q. Zhou, X. Wang, J. Zheng, X. Li, J. Mater. Chem. A 3 (2015) 16435–16439.
[97] Y. Liu, H. Jiang, Y. Zhu, X. Yang, C. Li, J. Mater. Chem. A 4 (2016) 1694–1701.
[98] G. Zhang, W. Lu, F. Cao, Z. Xiao, X. Zheng, J. Power Sources 302 (2016) 114–125.
[99] W. Yang, L. Chen, X. Liu, J. Jia, S. Guo, Nanoscale 9 (2017) 1738–1744.
[100] Y. Tu, H. Li, D. Deng, J. Xiao, X. Cui, D. Ding, M. Chen, X. Bao, Nano Energy 30 (2016) 877–884.
[101] Z. Wang, Y. Lu, Y. Yan, T.Y.P. Larissa, X. Zhang, D. Wuu, H. Zhang, Y. Yang, X. Wang, Nano Energy 30 (2016) 368–378.
[102] Y. Su, Y. Zhu, H. Jiang, J. Shen, X. Yang, W. Zou, J. Chen, C. Li, Nanoscale 6 (2014) 15080–15089.
[103] F. Lei, W. Liu, Y. Sun, J. Xu, K. Liu, L. Liang, T. Yao, B. Pan, S. Wei, Y. Xie, Nat. Commun. 7 (2016) 12697.
[104] J.-S. Li, B. Du, Z.-H. Lu, Q.-T. Meng, J.-Q. Sha, New J. Chem. 41 (2017) 10966–10971.
[105] W. Zhou, T. Xiong, C. Shi, J. Zhou, K. Zhou, N. Zhu, L. Li, Z. Tang, S. Chen, Angew. Chem. Int. Ed. 55 (2016) 8416–8420.
[106] J. Lu, W. Zhou, L. Wang, J. Jia, Y. Ke, L. Yang, K. Zhou, X. Liu, Z. Tang, L. Li, S. Chen, ACS Catal. 6 (2016) 1045–1053.
[107] Y. Yang, Z. Lin, S. Gao, J. Su, Z. Lun, G. Xia, J. Chen, R. Zhang, Q. Chen, ACS Catal. 7 (2016) 469–479.
[108] H.-X. Zhong, J. Wang, Q. Zhang, F. Meng, D. Bao, T. Liu, X.-Y. Yang, Z.-W. Chang, J.-M. Yan, X.-B. Zhang, Adv. Sustain. Syst. 1 (2017), 1700020.

[109] Y. Shen, Y. Zhou, D. Wang, X. Wu, J. Li, J. Xi, Adv. Energy Mater. 8 (2018), 1701759.
[110] H. Guo, N. Youliwasi, L. Zhao, Y. Chai, C. Liu, Appl. Surf. Sci. 435 (2018) 237–246.
[111] A. Sivanantham, S. Shanmugam, ChemElectroChem 5 (2018) 1937–1943.
[112] L. Zeng, X. Cui, L. Chen, T. Ye, W. Huang, R. Ma, X. Zhang, J. Shi, Carbon 114 (2017) 347–355.
[113] X. Zhong, Y. Qin, X. Chen, W. Xu, G. Zhuang, X. Li, J. Wang, Carbon 114 (2017) 740–748.
[114] J. Long, R. Li, X. Gou, Catal. Commun. 95 (2017) 31–35.
[115] S. Saha, A.K. Ganguli, ChemistrySelect 2 (2017) 1630–1636.
[116] Y. Yang, Z. Lun, G. Xia, F. Zheng, M. He, Q. Chen, Energy Environ. Sci. 8 (2015) 3563–3571.
[117] J. Yu, Y. Zhong, W. Zhou, Z. Shao, J. Power Sources 338 (2017) 26–33.
[118] G. Fu, Y. Chen, Z. Cui, Y. Li, W. Zhou, S. Xin, Y. Tang, J.B. Goodenough, Nano Lett. 16 (2016) 6516–6522.
[119] B. Bayatsarmadi, Y. Zheng, V. Russo, L. Ge, C.S. Casari, S.Z. Qiao, Nanoscale 8 (2016) 18507–18515.
[120] B. Du, Q.-T. Meng, J.-Q. Sha, J.-S. Li, N. J. Chem. 42 (2018) 3409–3414.
[121] S.H. Noh, M.H. Seo, J. Kang, T. Okajima, B. Han, T. Ohsaka, NPG Asia Mater. 8 (2016) e312.
[122] X. Duan, J. Xu, Z. Wei, J. Ma, S. Guo, S. Wang, H. Liu, S. Dou, Adv. Mater. 29 (2017).
[123] L. Dai, Y. Xue, L. Qu, H.J. Choi, J.B. Baek, Chem. Rev. 115 (2015) 4823–4892.
[124] J.P. Paraknowitsch, A. Thomas, Energy Environ. Sci. 6 (2013) 2839.
[125] D.-W. Wang, D. Su, Energy Environ. Sci. 7 (2014) 576.
[126] L. Yang, W. Zhou, J. Jia, T. Xiong, K. Zhou, C. Feng, J. Zhou, Z. Tang, S. Chen, Carbon 122 (2017) 710–717.
[127] J. Deng, L. Yu, D. Deng, X. Chen, F. Yang, X. Bao, J. Mater. Chem. A 1 (2013) 14868.
[128] M. Tavakkoli, T. Kallio, O. Reynaud, A.G. Nasibulin, C. Johans, J. Sainio, H. Jiang, E.I. Kauppinen, K. Laasonen, Angew. Chem. Int. Ed. 54 (2015) 4535–4538.
[129] J. Yu, W. Zhou, T. Xiong, A. Wang, S. Chen, B. Chu, Nano Res. 10 (2017) 2599–2609.
[130] H. Jin, J. Wang, D. Su, Z. Wei, Z. Pang, Y. Wang, J. Am. Chem. Soc. 137 (2015) 2688–2694.
[131] A. Aijaz, J. Masa, C. Rosler, W. Xia, P. Weide, A.J. Botz, R.A. Fischer, W. Schuhmann, M. Muhler, Angew. Chem. Int. Ed. 55 (2016) 4087–4091.
[132] J. Hou, Y. Sun, Y. Wu, S. Cao, L. Sun, Adv. Funct. Mater. 28 (2018) 1704447.
[133] H. Zhuang, Y. Xie, H. Tan, Y. Deng, Y. Li, G. Chen, Electrochim. Acta 262 (2018) 18–26.
[134] Y. Ma, X. Dai, M. Liu, J. Yong, H. Qiao, A. Jin, Z. Li, X. Huang, H. Wang, X. Zhang, ACS Appl. Mater. Interfaces 8 (2016) 34396–34404.
[135] X. Yan, L. Tian, M. He, X. Chen, Nano Lett. 15 (2015) 6015–6021.
[136] X. Yan, L. Tian, X. Chen, J. Power Sources 300 (2015) 336–343.
[137] Z. Wen, S. Ci, F. Zhang, X. Feng, S. Cui, S. Mao, S. Luo, Z. He, J. Chen, Adv. Mater. 24 (2012) 1399–1404.
[138] Y. Hou, T. Huang, Z. Wen, S. Mao, S. Cui, J. Chen, Adv. Energy Mater. 4 (2014) 1400337.
[139] Q. Wang, Y. Lei, Z. Chen, N. Wu, Y. Wang, B. Wang, Y. Wang, J. Mater. Chem. A 6 (2018) 516–526.
[140] X. Chen, J. Xiao, J. Wang, D. Deng, Y. Hu, J. Zhou, L. Yu, T. Heine, X. Pan, X. Bao, Chem. Sci. 6 (2015) 3262–3267.
[141] R.A. Sidik, A.B. Anderson, J. Phys. Chem. B 110 (2006) 936–941.
[142] J. Yang, G. Zhu, Y. Liu, J. Xia, Z. Ji, X. Shen, S. Wu, Adv. Funct. Mater. 26 (2016) 4712–4721.
[143] X. Zhang, S. Liu, Y. Zang, R. Liu, G. Liu, G. Wang, Y. Zhang, H. Zhang, H. Zhao, Nano Energy 30 (2016) 93–102.
[144] R. Li, Y. Dai, B. Chen, J. Zou, B. Jiang, H. Fu, J. Mater. Chem. A 307 (2016) 1–10.
[145] Y. Hao, Y. Xu, W. Liu, X. Sun, Mater. Horiz. 5 (2018) 108–115.
[146] J. Tian, Q. Liu, A.M. Asiri, X. Sun, J. Am. Chem. Soc. 136 (2014) 7587–7590.
[147] Q. Liu, J. Tian, W. Cui, P. Jiang, N. Cheng, A.M. Asiri, X. Sun, Angew. Chem. Int. Ed. 53 (2014) 6710–6714.
[148] E.J. Popczun, C.G. Read, C.W. Roske, N.S. Lewis, R.E. Schaak, Angew. Chem. Int. Ed. 53 (2014) 5427–5430.
[149] Q. Jin, B. Ren, D. Li, H. Cui, C. Wang, Nano Energy 49 (2018) 14–22.
[150] W. Xia, R. Zou, L. An, D. Xia, S. Guo, Energy Environ. Sci. 8 (2015) 568–576.
[151] Z. Li, M. Shao, L. Zhou, R. Zhang, C. Zhang, M. Wei, D.G. Evans, X. Duan, Adv. Mater. 28 (2016) 2337–2344.
[152] Y.V. Kaneti, J. Tang, R.R. Salunkhe, X. Jiang, A. Yu, K.C. Wu, Y. Yamauchi, Adv. Mater. 29 (2017) 1604898.
[153] J. Liu, D. Zhu, C. Guo, A. Vasileff, S.-Z. Qiao, Adv. Energy Mater. 7 (2017) 1700518.
[154] A.A. Gewirth, J.A. Varnell, A.M. DiAscro, Chem. Rev. 118 (2018) 2313–2339.
[155] M. Zhou, H.L. Wang, S. Guo, Chem. Soc. Rev. 45 (2016) 1273–1307.
[156] B.Y. Guan, X.Y. Yu, H.B. Wu, X.W.D. Lou, Adv. Mater. 29 (2017) 1703614.
[157] H.B. Yang, J. Miao, S.F. Hung, J. Chen, H.B. Tao, X. Wang, L. Zhang, R. Chen, J. Gao, H.M. Chen, L. Dai, Sci. Adv. 2 (2016) e1501122.
[158] G. Fu, Z. Cui, Y. Chen, Y. Li, Y. Tang, J.B. Goodenough, Adv. Energy Mater. 7 (2017) 1601172.
[159] X. Han, X. Wu, C. Zhong, Y. Deng, N. Zhao, W. Hu, Nano Energy 31 (2017) 541–550.
[160] J. Zhang, Z. Zhao, Z. Xia, L. Dai, Nat. Nanotechnol. 10 (2015) 444–452.